Constraints on the porosity, permeability and porous micro-structure of highly-crystalline andesitic magma during plug formation

Amelia A. Bain*[1], Anthony Lamur[2], Jackie E. Kendrick[2], Yan Lavallée[2], Eliza S. Calder[1], Joaquín A. Cortés[3], Ian B. Butler[1], Gloria Patricia Cortés[4]

[1] School of Geosciences, Grant Institute, University of Edinburgh, James Hutton Road, Edinburgh EH9 3FE, UK

[2] School of Environmental Sciences, Jane Herdman Building, University of Liverpool, 4 Brownlow Street, Liverpool L3 5DA, UK

[3] Department of Geography, Edge Hill University, St Helens Road, Ormskirk, Lancashire L39 4QP, UK

[4] Servicio Geológico Colombiano, Observatorio Vulcanológico y Sismológico de Manizales, Manizales, Avenida 12 de Octubre No. 15-47, Caldas, Colombia

* Corresponding author. E-mail address: Amelia.Bain@ed.ac.uk

Abstract

The development of pore overpressure beneath high-crystallinity, low-permeability magma plugs is often inferred to be the cause of hazardous vulcanian explosions at many active arc volcanoes. Using a combination of porosity and permeability measurements and X-ray micro-tomographic reconstructions of ballistic bombs from the 2004-2010 explosions of Galeras volcano, Colombia, we document the micro-structural changes of the permeable porous network in high-crystallinity andesitic magma plugs resulting from natural viscous densification. Mean pore volumes, mean pore throat areas and the volumetric number density of connected pores and throats decline as connected porosity and permeability decrease. The mean pore coordination number and the volumetric number density of disconnected (isolated) voids also tend to decrease with decreasing porosity and permeability. The variance in pore volume and throat area decrease as a result of this densification process and tortuosity decreases slightly, demonstrating that the range of scales of structures performing gas transfer is reduced and the porous network undergoes viscous re-organisation. The reduction in tortuosity illustrates how permeability is reduced but maintained to low connected porosities, allowing plug formation to occur without creating large-scale pore overpressure within the plug. We characterise the relationships between key topological parameters and between connected porosity and permeability to facilitate future modelling of this process. Micro-tomographic reconstructions of a breadcrust bomb rind indicate that a deeper region with large pores, large throats, high pore volume and throat area variance and high tortuosity exists below low-permeability plugs, and this could represent a likely area for explosion-driving overpressure to develop following plug densification. A comparison of our porous micro-structure data with existing crystal micro-textures and glass volatile data from the same samples suggests that the

average magma ascent and decompression rates ultimately control the efficiency of magma densification, the final plug permeability and the extent of degassing of the melt phase.

Keywords

Plug, Porosity, Permeability, Micro-tomography, Densification, Vulcanian explosion

1. Introduction

Sequences of repeated, or cyclical, vulcanian explosions represent a frequent expression of andesitic-dacitic volcanism at arc volcanoes worldwide (e.g. Clarke et al., 2007; Hammer et al., 1999; Lavallée et al., 2012; Stix et al., 1997; Voight, 1999; Wright et al., 2007). These spontaneous explosions result from the emplacement of high-crystallinity, low-permeability plugs of degassed magma in the shallow conduit (<500 m, Fig. 1) (Bain et al., 2019; Clarke et al., 2007; Giachetti et al., 2010; Hammer et al., 1999; Sparks, 1997; Stix et al., 1997; Voight, 1999; Wright et al., 2007). Further degassing beneath these low-permeability plugs triggers explosions when the strain rate exerted by overpressure in gas bubbles overcomes the structural relaxation rate of the magma (Clarke, 2013; Clarke et al., 2007; Coats et al., 2018; Dingwell, 1996; Lavallée et al., 2012; Sparks, 1997; Stix et al., 1993). The formation of such degassed, low-permeability plugs is intimately linked to the processes of melt degassing, crystallisation and magma outgassing during magma ascent (Bain et al., 2019; Cashman and Blundy, 2000; Hammer et al., 2000, 1999; Lavallée et al., 2012; Preece et al., 2016). Tracking the evolution of porosity and permeability in ascending magmas is therefore fundamentally important for building understanding of eruption dynamics, improving ascent models and successful eruption forecasting.

Whereas the development of porosity, via magma vesiculation and strain, and the attainment of the percolation threshold (the threshold porosity at which magma ceases to be impermeable to gas) control the timing of permeability development, gas permeability itself controls the rate of gas loss and determines eruption style through the development or dissipation of pore pressure (Burgisser et al., 2017; Eichelberger et al., 1986; Okumura et al., 2009). As gas permeability is known to strongly depend on the topology of the porous network (Burgisser et al., 2017; Colombier et al., 2017; Degruyter et al., 2010; Gonnermann et al., 2017; Mueller et al., 2005; Saar and Manga, 1999; Wadsworth et al., 2017; Wright et al., 2009, 2006; Yokoyama and Takeuchi, 2009), the micro-structural properties of densifying magma subjected to shear and compaction hold key information regarding the timing and distribution of permeability reduction in densifying magma plugs. The spatial distribution of these properties determines whether gas escapes and pore pressures are reduced, or local pressurisation and fragmentation occurs at small-scales, possibly resulting in the formation of tuffisite veins (e.g. Kendrick et al., 2016) and the occurrence of ash venting (Cassidy et al., 2018, and references therein), or whether larger portions of the plug (and possibly lava dome) are expelled in a vulcanian explosion resulting from the development of large-scale pore overpressure (e.g. Lavallée et al., 2012; Sato et al., 1992).

This study aims to track the reduction of porosity and permeability during andesitic magma densification and plug formation in a well-constrained natural system and link these macroscopic properties with the micro-scale topological evolution of the porous network. In this work, we measure the porosity and permeability of andesitic ballistic bombs produced by vulcanian explosions of the 2004-2010 eruptive period of Galeras volcano, Colombia, and analyse the topology of the porous network in the pyroclasts using X-ray micro-tomography. These ballistics sample portions of the degassed (<0.4 wt% H_2O), densified magma plugs emplaced at shallow levels (<500 m) prior to vulcanian explosions (Fig. 1) (Bain et al., 2019)

and therefore provide snapshots of the porosity, permeability and micro-structure of high-crystallinity andesitic magma at various stages of densification. We characterise the porosity-permeability relationship preserved in this sample suite and present detailed characteristics of the geometry of the collapsing porous network in order to track the micro-structural evolution of densifying andesitic plugs. We also analyse the pore structure of a sample of partially-annealed tuffisite vein material preserved in a dense ballistic bomb in order to compare the characteristics of the host andesitic plug and the material filling tuffisite veins, which are increasingly inferred to represent high-permeability pathways for gas transfer (Berlo et al., 2013; Castro et al., 2012; Kendrick et al., 2016; Kolzenburg et al., 2012). Finally, we compare this dataset with previously published crystal micro-texture and groundmass glass data from the same samples (Bain et al., 2019) and propose a conceptual model of plug formation linking magma decompression and densification rates.

2. Background

Much work has focussed on the onset and evolution of permeability and the controls on the percolation threshold during magma vesiculation (Burgisser et al., 2017; Colombier et al., 2017; Degruyter et al., 2010; Gonnermann et al., 2017; Klug and Cashman, 1996; Lindoo et al., 2017; Rust and Cashman, 2004; Saar and Manga, 1999; Takeuchi et al., 2005; Wright et al., 2006, 2009). Changes in porosity and permeability during densification have been studied in crystal-poor magma (Ashwell and Kendrick et al., 2015; Gonnermann et al., 2017; Kennedy et al., 2016) and initially granular volcanic materials, e.g. welding ignimbrites (Heap et al., 2015; Wright and Cashman, 2014) and sintering crystal-free (Wadsworth et al., 2016) and crystal-rich (Kendrick et al., 2016) droplets. However, comparatively less is known regarding the

120 evolution of porosity and permeability during the densification of high-crystallinity magma, a
121 process that is key to understanding the formation of low-permeability plugs, effusive-
122 explosive transitions and the timing and magnitude of vulcanian explosions. Recent studies
123 examining the process of magma densification under isotropic stress have shown that
124 permeability is only slightly reduced by surface tension over relatively long periods of time,
125 and the densification process is further lengthened by the presence of crystals (Kennedy et al.,
126 2016; Okumura et al., 2013). Similarly the presence of crystals in initially granular densifying
127 materials delays the sintering process, which can influence the development of pressurisation
128 and gas-and-ash explosion cycles (Kendrick et al., 2016). Further studies involving the high-
129 temperature (anisotropic) compression of near-aphyric pumice showed more efficient closure
130 of void space and a corresponding decrease in permeability and increase in permeability
131 anisotropy (parallel and perpendicular to shear), but the application of shear stress failed to
132 completely close the pore space in even relatively crystal-poor magmas, which compacted to a
133 threshold porosity (Ashwell and Kendrick et al., 2015). Experimental work on high-
134 crystallinity andesites has shown that magma rheology evolves variably during shear, as at high
135 strain rates shear may trigger dilation and creation of pore space via tearing and fracturing
136 (Lavallée et al., 2013) or compaction of the porous network, via pore flattening and closure
137 (Heap et al., 2017; Kendrick et al., 2013). Thus, both the degree of densification and the
138 timescale over which it occurs may be intrinsically linked to the stress field, and hence the
139 depth at which a magma plug forms.

140 Many studies have suggested the existence of a hysteresis in the porosity-permeability
141 relationship in magma (e.g. Saar & Manga 1999; Rust & Cashman 2004; Wright et al. 2009;
142 Michaut et al. 2009; Gonnermann et al. 2017). Permeability development during vesiculation
143 is thought to occur once a system-spanning permeable pathway develops at the onset of the
144 percolation threshold. The percolation threshold itself may depend on many factors, such as

145 composition, crystallinity and strain history. During densification, higher permeability may be
146 maintained to low values of porosity by retaining bubble interconnections that may not exist at
147 a similar porosity during vesiculation, due to the nature of densification (Kennedy et al., 2016),
148 the presence of micro-fractures (Kushnir et al., 2017; Mueller et al., 2005), and the presence of
149 crystals that hinder the closure of pores (Ashwell and Kendrick et al., 2015; Kennedy et al.,
150 2016) and enhance the opportunity for bubble interconnections (Laumonier et al., 2011; Lindoo
151 et al., 2017). As a result, porosity-permeability evolution paths during vesiculation and
152 densification may differ significantly (Ashwell and Kendrick et al., 2015; Colombier et al.,
153 2017; Gonnermann et al., 2017; Rust and Cashman, 2004; Saar and Manga, 1999; Wright et
154 al., 2009). Michaut et al. (2009) showed that taking account of hysteretic permeability in
155 magma ascent models could generate low-permeability plugs over a short distance, illustrating
156 the importance of constraining the micro-structural processes that control permeability
157 reduction in densifying magma to improve existing ascent models.

158

159 **3. Materials & Methods**

160

161 3.1 Sample selection

162

163 For permeability and porosity measurements, nineteen andesitic ballistic bombs from the 2004-
164 2010 period of activity of Galeras volcano were collected from the caldera rim with the
165 assistance of the Geological Survey of Colombia (Servicio Geológico Colombiano, SGC). The
166 stratified nature of magma plugs at Galeras volcano gave rise to three types of ballistic bombs
167 as a result of the competition between syn-eruptive quenching and interior vesiculation of the
168 pyroclast (Fig. 1), as described in Bain et al. (2019). The water content of the melt phase in
169 magma that produced dense and scoriaceous bombs was too low (<0.4 wt% H_2O; Bain et al.,

2019) to result in vesiculation on eruptive timescales (Hoblitt and Harmon, 1993; Wright et al., 2007) due to the speciation of water in rhyolitic melt at very low water contents, comprising primarily hydroxyl groups rather than molecular water available to partition into the vapour phase (Silver et al., 1990). Hence, dense and scoriaceous bombs are considered to adequately preserve pre-eruptive magma textural properties such as vesicle size and shape, as well as porosity and permeability, with the caveat that overprinting modifications to the porous network may have been sustained due to strain during bomb flight and impact. Inflated bombs typically have a bread-crusted morphology due to higher melt water contents (>0.4 wt% H_2O; Bain et al., 2019) that allowed them to partially vesiculate on eruptive timescales, resulting in a pumiceous interior due to vesiculation and a dense rind due to quenching and a syn-eruption bubble nucleation delay (Wright et al., 2007). Hence, in the case of inflated bombs, only the dense rind adequately preserves the pre-eruptive magma properties. In this study, we focus on the dense and scoriaceous bombs that did not vesiculate upon explosive decompression as we probe the pre-eruptive properties of the most degassed part of the plugs. These bombs can be identified in the field by their dense appearance and lack of bread-crusted morphology (Fig. 1).

Among the dense and scoriaceous bombs selected, ballistics covering the full range of porosities observed in the field were collected so as to give the most detailed representation of samples through the average andesitic plug at Galeras volcano. Connected porosity and permeability measurements were performed on these nineteen samples. Eight of these samples covering the range of measured porosities were then selected for X-Ray micro-tomography to investigate the topology of the porous network. Micro-tomography data were also collected for nine additional dense and scoriaceous samples from the study of Bain et al. (2019), six of which have known eruption dates, quantified feldspar micro-textures and glass volatile analyses. One sample from the dense rind of a breadcrust (inflated) bomb was also found to be suitable for micro-tomography, as it was un-fractured and thick enough to provide a sufficient volume.

195 Finally, a sample of tuffisite material from a vein hosted in a dense bomb was also imaged by
196 micro-tomography to compare the nature of the porous network in tuffisites and the host
197 andesite (comprising dense bombs, scoriaceous bombs and the breadcrust bomb rind). Table 1
198 lists the samples used in this study and the analyses performed.

199

200 3.2 Porosity and permeability measurements

201

202 All porosity and permeability measurements were conducted in the Experimental
203 Volcanology and Geothermal Research Laboratory at the University of Liverpool. 26 mm-
204 diameter cores were produced from the selected bomb samples. Most samples appeared
205 isotropic but cores were cut perpendicular to the direction of vesicle elongation in two
206 samples where this was visually discernible (GAL9 & GAL16). The ends of each core were
207 then ground parallel to lengths ranging 40.66-54.33 mm. Cores were washed in an ultrasonic
208 bath and oven-dried overnight at 70 °C. The fraction of connected pores (connected porosity),
209 ϕ_c, of each core was quantified by gas displacement pycnometry using an AccuPyc 1340
210 helium pycnometer developed by Micromeritics. This instrument measures the skeletal
211 volume of the sample (i.e. the fraction of rock and isolated pores), V_s, with an accuracy of
212 ±0.1 %. Together, this volume and the geometrical volume of a core specimen, V_c, may be
213 used to compute the fraction of connected pores via: $\phi_c = (V_c - V_s)/V_c$. The propagated
214 uncertainty on our measurements of connected porosity is ±0.8 %, taking into account the
215 error on the sample measurements (assumed to be ±0.01 mm) and the error on the measured
216 skeletal volume.

217 Darcian (laminar) permeability, k, at confining pressures of 0.7, 1.4 and 2.1 MPa was
218 determined for each sample using a steady-state nitrogen gas permeameter (GasPerm)

developed by Vinci technologies and the constant flow-rate method. For this set-up, samples are placed within a chamber housing a rubber sleeve surrounded by nitrogen gas to control the confining pressure applied onto the sample. The instrument then varies the flow rate of nitrogen across the sample until the inlet pressure stabilises (with fluctuations smaller than 0.0004 MPa/min). Whilst the flow rate is held steady, the inlet and outlet pressure (in this case, atmospheric conditions) are monitored, in order to calculate the permeability using Darcy's Law (Darcy, 1857, 1856). Additionally, both Forchheimer (Whitaker, 1996) and Klinkenberg coefficients (Klinkenberg 1941) are calculated to determine the maximum allowable flow rate that satisfies Darcy conditions (meaning laminar flow conditions are satisfied and no gas slippage occurs along the walls of the void space). The propagated uncertainty associated with our permeability measurements is ±3 %, taking into account the accuracy of the gas flow meter and the pressure transducer on the GasPerm instrument. We acknowledge that the permeability of magma and that of the solid pyroclasts that we measure, produced from the quenching of fragmented magma plugs, will not be identical. However, as it is currently technically and financially challenging to measure the permeability of high-temperature magma samples and as we are interested in the changes in permeability across the sample set, we use the permeability range of our solid ballistic bomb samples to represent the range of magma permeability within the Galeras plugs.

3.3 Vesicle textures

Cylindrical cores of rock 8 mm in diameter were drilled from each sample selected for micro-tomography. These cores were drilled parallel to the long axis of the larger cores used for porosity and permeability measurements for the samples where these were measured. For the inflated bomb rind sample, a core was drilled from the dense rind and this core did not include

any material from the vesicular bomb interior. The cores were then washed in an ultrasonic bath for a period of several minutes and were oven-dried overnight.

X-ray micro-tomography was carried out in the Experimental Geosciences Facility at the University of Edinburgh. Cores were scanned using a cone beam geometry and a peak X-ray energy of 120 keV. A 0.8 mm thick aluminium energy filter was positioned between the sample and the camera to reduce beam hardening effects. For each scan, 1500-2000 projections were acquired through a 360° rotation, each with an exposure time of 1 s. Tomographic slices were reconstructed from the projections using Octopus v8.9 software (Dierick et al., 2004). During reconstruction, a further beam hardening correction and a filter for ring artefacts were applied. Reconstructed slices of the scanned volume consist of tiff files of 16 bit greyscale images (examples are shown in Fig. 5). The pixel resolution of these images ranged from 7.754-10.736 μm and the "real" resolution of objects in the resulting data volume (considered to be two voxel lengths for practical purposes) ranged from 15.508-21.472 μm (Supplementary File A).

The topology of the porous network was examined by following the method of Degruyter et al. (2010). The sequences of reconstructed greyscale images of each sample were first cropped using ImageJ software (Schneider et al., 2012) to produce a prismatic data volume. ImageJ was also used to examine histograms of the images' greyscale to select appropriate thresholds to bracket the void and solid phases (the solid phase here consists mainly of glass, feldspar, pyroxene and Fe-Ti oxide crystals, Bain et al., 2019). The 3DMA-Rock code of Lindquist & Venkatarangan (1999) was then used to analyse the 3-D spatial characteristics of the porous network.

The data volume was first segmented, meaning each voxel was classified as either solid or pore phase, using the two-pass indicator kriging algorithm implemented in the 3DMA-Rock program (Oh & Lindquist 1999; Lindquist & Venkatarangan 1999). The first pass utilises the threshold values extracted from ImageJ to assign most of the voxels to the solid or void phase.

The second pass utilises an indicator kriging method to assign the remaining voxels to one of the phases, based on the spatial covariance of the image and a minimum variance estimation (Oh & Lindquist 1999). The process of segmentation produces a new binary data volume in which voxels belonging to the void phase can be studied as a numerical porous network (Degruyter et al., 2010). It is challenging to estimate the uncertainty in our segmentation in the absence of a reference sample with known properties. We therefore estimated an error of ±2.2 % on the total volume of our segmented pore space, based on the volume difference after applying opening and closing operations to the segmented pore volume for one sample (AB23). These operations smooth out the effects of the misclassification of voxels and provide a reasonable estimate of the magnitude of the error as most of the uncertainty originates from the misclassification of the small-scale features modified by opening and closing operations.

Once segmented, isolated pores smaller than 10 voxels and all isolated grain phase voxels were removed in a cleaning procedure, to provide a lower limit for the resolution of the disconnected voids (equivalent to 10^{-6}-10^{-5} mm^3, Supplementary File A) and to remove artificial isolated grains in the data volume, respectively. The medial axis, or skeleton, of the connected pore structure of each sample was then obtained. The skeleton is a simplified representation of the topology of the porous network and preserves its key geometric characteristics whilst facilitating its analysis. The skeletonisation process uses an erosion method to remove pore space voxels layer by layer from the exterior of the connected pore space object until a chain of single, connected voxels remains (Lee et al., 1994). The skeleton can then be used as a reference structure to identify specific sites in the porous network, such as branching points (nodes) or pore apertures (throats). Nodal pores correspond to vertices on the medial axis where several pore pathways meet. The 3DMA-Rock package employs a vertex merging algorithm ensuring that a nodal pore is identified as such despite the fact that it may have more than one

293 vertex lying within it. Once merged, these nodal pores have a coordination number
294 corresponding to the number of connecting pores, which is a property of interest.

295 Where possible (i.e. where connecting paths existed) the geometric tortuosity of the porous
296 network was estimated in 3DMA-Rock by calculating the shortest paths from influx to outflux
297 along the three dimensions of the data volume (x, y and z directions, where the z direction
298 corresponds to the long axis of cores used for connected porosity and permeability
299 measurements). The tortuosity for each direction is calculated as the median of the geometric
300 tortuosity along each possible connecting path. Pore throats were identified by creating a
301 distance map from the medial axis to the closest grain surface. Pore throats consist of the area
302 within the minimum closed loop linking contact points between each pore pathway edge (the
303 contact between the void and solid phases) and a cylinder that is progressively expanded by
304 dilation from the skeleton, on each segment of the medial axis linking nodal pores. The pore
305 throat surface area is the minimum surface area defined by this closed loop (Fig. 2). The
306 resulting pore network model consists of pores with associated volumes and coordination
307 numbers, separated by pore throat surfaces with associated areas. Effective throat and pore
308 radii were also calculated as the equivalent circular and equivalent spherical radii, respectively.

309

310 **4. Results**

311

312 4.1 Porosity and permeability of bomb samples

313

314 The permeability of the variably porous samples was measured at different confining pressures
315 (Fig. 3, Table 1, Supplementary File B) within the range of magma storage pressures calculated
316 for dense and scoriaceous bombs in the study of Bain et al. (2019). Darcy conditions were

achieved while measuring the permeability of all samples but GAL10, for which the Klinkenberg-corrected permeability was used to account for gas slippage along pore walls (Klinkenberg 1941), following the method described by Heap et al. (2018). We find that at a given confining pressure, measured permeability, *k*, is typically higher for samples with higher connected porosities, ϕ_c (Fig. 3, Table 1). For each sample, measured permeability decreases with increasing confining pressure (Fig. 3). Samples with lower connected porosity ($\phi_c \lesssim 10$ %) and permeability tend to show a greater dependence of the permeability on confining pressure. Overall, permeability varies over five orders of magnitude (1.13×10^{-16} – 1.63×10^{-12} m^2 over the range of applied confining pressures) and connected porosity varies from 1.9-26.3 % (Fig. 3), consistent with qualitative observations from thin sections (Fig. 4).

Despite the overall trend of higher permeability corresponding to samples with higher connected porosity, we note important distinctions in the permeability of certain samples with similar porosities. At a given confining pressure, samples GAL6, GAL8, GAL13 and GAL19 (boxes in Fig. 3) have notably higher permeabilities (up to two orders of magnitude) than samples GAL2, GAL4, GAL9, GAL12, GAL16 with similar connected porosities (Table 1). This set of comparatively "higher-permeability" samples also shows a notably smaller dependence on confining pressure than samples with lower permeability and similar ϕ_c, as well as samples with lower ϕ_c (Fig. 3, Supplementary File B). Eight samples covering the full range of ϕ_c were selected for further exploration by micro-tomography (Table 1), including two low/high permeability pairs with similar connected porosities (GAL4/GAL6 & GAL16/GAL8) in order to investigate any topological controls on the observed permeability difference.

4.2 Quantification of vesicle textures

341 Samples with higher connected porosity correspond to samples with a higher areal void fraction
342 when observed in thin section (Fig. 4). Vesicles are typically polylobate and/or branching in
343 shape (Fig. 4), as previously described by Bain et al. (2019). Examples of reconstructed
344 tomographic slices through the scanned cores are shown in Fig. 5 and illustrate the
345 fundamentally different nature of the porous network in the host andesite (comprising dense
346 bombs, scoriaceous bombs and the breadcrust bomb rind; Fig. 5a–c), which consists of
347 interconnected, branching vesicles, and in the sample of tuffisite material (Fig. 5d), which
348 consists of voids between partially sintered granular material. Fig. 6 shows examples of the
349 rendered pore space and the corresponding pore network models in host andesite samples and
350 the tuffisite sample.
351 Analysed micro-tomography data volumes ranged from 274–473 mm^3. Among the samples for
352 which connected porosity was measured, numerical porosities computed from the micro-
353 tomography data, which represent the total porosity for a sample, ranged from 0.2–25.9 %. The
354 numerical porosities obtained are generally in good agreement with the range in measured
355 connected porosities (Fig. 7). Numerical porosity typically underestimates the measured
356 connected porosity by up to 5% due to the resolution limit of the micro-tomography (see section
357 3.3). However, as this difference is small, non-systematic and relatively consistent, numerical
358 porosity values are considered to provide an adequate measure of sample porosity for the
359 purposes of investigating changes in the topology of the void space, and we use this as a metric
360 to track the extent of densification.
361 Although the distributions of pore volumes, throat surface areas and pore coordination numbers
362 computed for each sample are non-normal (Supplementary File C), we use the arithmetic mean
363 of these distributions as an average value for each parameter that is a skewed representation of
364 the central tendency taking into account the distribution tails (e.g. outlying larger pores and
365 larger throats that are progressively closed as a result of densification). Median values for these

366 distributions do not vary significantly from the means (Supplementary File C) but do not
367 capture the tails, which are expected to be important in understanding the densification process.
368 Although there is some scatter in our data (Fig. 8), we describe the general trends here through
369 best-fitting relationships (on the basis of the lowest root mean square error, RMSE) and discuss
370 the possible causes of scatter in section 5.1. The RMSE for each best-fit relationship is given
371 in Fig. 8 and the equations and RMSEs for all attempted fits are given in Supplementary File
372 A.

373 Among the samples of host andesite, the mean pore volume and mean throat area show power
374 law relationships with numerical porosity (Fig. 8a–b), and samples with lower numerical
375 porosity tend to have lower mean pore volumes and mean throat areas. The rate of decrease in
376 the mean pore volume and mean throat area with decreasing numerical porosity is relatively
377 low above a porosity of around 10 %, and higher below this porosity (Fig. 8a–b). The
378 volumetric number densities of connected pores (Fig. 8c) and of connected throats (Fig. 8d)
379 each show an exponential relationship with numerical porosity, with lower porosities
380 corresponding to lower number densities of pores and throats. The mean pore coordination
381 number shows a power law relationship with numerical porosity (Fig. 8e). As for the mean
382 pore volume and throat area, the rate of decrease of the mean coordination number with
383 porosity is low above a porosity of around 10 % and higher below this porosity. The mean
384 coordination number drops below 1 at a threshold porosity of around 0.5 % (Fig. 8e), meaning
385 pores are typically isolated below this porosity. The volumetric number density of disconnected
386 voids (defined as the average number of disconnected voids per mm^3 of analysed material) also
387 displays a poorly-defined power law relationship with numerical porosity, with a large amount
388 of scatter in the porosity range 5–15% (Fig. 8f). The variance in connected pore volumes and
389 throat areas is also higher in samples with higher numerical porosity (Fig. 8g–h). There is a
390 strong positive relationship between the mean effective pore and mean effective throat radii

(Fig. 9). Tortuosity is slightly higher (>2.5) in samples with a mean pore volume above 0.06 mm^3 (Fig. 10a) and is similar (2–2.5) for lower pore volumes. The lowest tortuosity observed in each sample decreases slightly with mean pore throat area (Fig. 10b) except for sample GAL8, and the range of tortuosity (2–2.6) is similar for pore throat areas in the range 1.1–1.7 $\times 10^4$ μm^3. Tortuosity shows no clear relationship with the mean coordination number in each sample (Fig. 10c). The sample with the highest tortuosity and the highest anisotropy with respect to paths tortuosity in the x, y and z directions is the rind of the breadcrust bomb sample.

Among samples for which connected porosity and permeability were measured (Table 1), the volumetric number density of pores, throats and disconnected voids, and the ratio of the number of throats to the number of pores (normalised by the analysed volume), are typically higher in samples with higher measured connected porosity and permeability (Fig. 11). The mean coordination number of each pore, the mean pore volume and mean throat surface area are also typically higher in samples with higher measured porosity and permeability (Fig. 11). Tortuosity is slightly higher in samples with higher measured porosity and permeability, although GAL16 shows a higher tortuosity than the other samples and GAL8 shows notably higher tortuosity in the y direction, resulting in some scatter. All micro-tomography analysis results are provided in Supplementary File A.

The sample taken from a tuffisite vein hosted in a dense bomb ($AB2_T$) is characterised by much higher volumetric number densities of connected pores and throats (Fig. 8c–d). The mean pore volume and throat area in the tuffisite are also lower than in the host andesite for a similar porosity (Fig. 8a–b). The variance in pore volumes and the variance in throat areas are also very low in this sample (Fig. 8g–h). The mean pore coordination number in the tuffisite is on the higher end of the dataset and this material also features a high number density of disconnected voids (Fig. 8e–f). Tortuosity is among the lowest in the dataset for this sample (Fig. 10). The relationship between the effective throat to pore radii in this material fits with

416 the overall trend of the host andesite data (Fig. 9), but both these effective radii are on the
417 smaller end of the dataset as a whole.

418

419 4.3 Low/high permeability pairs of samples with similar connected porosity

420

421 Two pairs of samples, GAL4/GAL6 and GAL16/GAL8, with similar measured connected
422 porosities ($\Delta\phi_c$< 1%) but permeabilities varying by two orders of magnitude (Table 2) were
423 selected for micro-tomography in order to investigate any topological controls on the observed
424 permeability difference. In both pairs the mean coordination number and volumetric number
425 density of disconnected (isolated) voids are similar (Table 2).

426 In the case of pair GAL4/GAL6, the higher permeability sample (GAL6) shows a higher
427 volumetric number density of pores and throats than the low permeability sample, and higher
428 mean effective pore and mean effective throat radii (Table 2). The higher permeability sample
429 also displays a lower variance in pore volumes and throat areas (Table 2). Tortuosity could not
430 be established for the low permeability sample as there were no volume-spanning connected
431 paths in the x, y and z directions and therefore tortuosity could not be compared for this pair of
432 samples. In the case of pair GAL16/GAL8, the higher permeability sample (GAL8) has a lower
433 number density of pores and throats than the low permeability sample (Table 2). Both samples
434 exhibit a similar mean throat area and a similar variance in throat areas but the higher
435 permeability sample has a slightly lower mean pore volume and lower variance in pore volumes
436 (Table 2). Geometric tortuosity is higher in the low permeability sample in the x and z
437 directions (with z representing the direction in which permeability was measured), and higher
438 in the high permeability sample in the y direction (Table 2).

439

5. Discussion

5.1 Topology of the porous network

The combination of micro-tomography data and porosity and permeability measurements illuminates the topological changes in the porous network associated with magma densification in the Galeras plugs. We observe that magma densification (total porosity covering the range 25.9–0.1 %) is accompanied by the progressive reduction of mean pore volume (7.84×10^{-2} – 2.98×10^{-4} mm^3), mean throat surface area (2.47×10^4 – 1.1×10^3 μm^2) and mean pore coordination number (4.37–0.42) as connected porosity (26.3–1.9 %) and permeability (1.63×10^{-12} – 1.13×10^{-16} m^2) decline. The variance in pore volumes and throat areas is also reduced (4.12×10^{-2} – 3.89×10^{-6} mm^6 and 8.31×10^9 – 1.91×10^6 μm^4, respectively), implying that the range of length-scales of the structures performing gas transfer at the sample-scale (pores and throats) becomes smaller. The porous medium therefore becomes more homogeneous during densification as the range of pore volumes and throat sizes decreases. The volumetric number density of connected pores (2.69×10^1– 1.69×10^{-1} mm^{-3}) and throats (6.90×10^1– 2.58×10^{-1} mm^{-3}) and the volume-normalised ratio of throats to pores (3.17–0.22) also decline as a result of densification.

Interestingly, the number density of disconnected voids is also generally reduced (94.27–1.43 mm^{-3}) despite a large amount of scatter in the data (Fig. 8f & Fig. 11), suggesting that the closure and/or coalescence of isolated pores with the connected porous network typically proceeds more efficiently than the creation of new isolated pores by throat closure. We speculate that the scatter in the disconnected voids dataset, as well as in other micro-tomography datasets, could attest to differences in the amount of strain, nature of strain, or the strain rate experienced by different parcels of magma in the conduit, as high strain rates closer

to the conduit margins are likely to promote bubble coalescence (Okumura et al., 2009). The scatter in the mean pore volume and mean throat area datasets may also be related to syn-eruptive deformation of the porous network during magma fragmentation, bomb flight and impact.

The decrease in tortuosity (3.57–2.11, considered as the average tortuosity in the x, y and z directions) as mean pore volume and mean throat area are reduced shows that more direct gas transfer pathways are created as a result of densification, implying that permeability is maintained during densification until very low porosities, as observed in the permeability measurements and in previous studies (Ashwell and Kendrick et al., 2015; Gonnermann et al., 2017; Heap et al., 2015; Kendrick et al., 2013; Kennedy et al., 2016; Okumura and Sasaki, 2014). As the number densities of pores and throats typically decline during this process, implying that bubbles and bubble connections are progressively lost (Fig. 8c–d & Fig. 11), we suggest that these more direct pathways result from the rearrangement of pores and throats, as well as bubble coalescence, during viscous deformation of the magma plug and, thus, of the porous network. We also note that the number density of connected pores appears to decline at a lower rate as a result of densification than the number density of throats until very low porosities (2–3%) are attained (Fig. 8c–d), suggesting the importance of the concerted processes of throat closure, formation of disconnected voids, and connection of disconnected voids to the connected porous network.

Micro-tomography data from the sample taken from a tuffisite vein preserved in a dense bomb show that the average pore volume and pore throat surface area are much smaller in the tuffisite material than in the host andesite (Fig. 8a–b), confirming qualitative observations from the reconstructed tomographic slices (Fig. 5). The number densities of pores and throats are much higher in the tuffisite (Fig. 8c–d), the mean coordination number is among the highest in the dataset (Fig. 8e) and the tortuosity is among the lowest in the dataset (Fig. 10). The number

490 density of disconnected voids is comparatively high, and the variance in pore volume and in
491 throat area are both very low (Fig. 8f–h). These data show that the porous network in the
492 tuffisite vein material is characterised by small, well-connected pores and throats with narrow
493 size-distributions, between ash-size fragments of andesite. Despite the small throat sizes, this
494 material features more direct pathways for gas transfer due to the low tortuosity, which may
495 constitute the primary reason that tuffisites represent high-permeability pathways despite the
496 small scale of the micro-structures performing gas transfer (Berlo et al., 2013; Castro et al.,
497 2012; Kendrick et al., 2016; Kolzenburg et al., 2012; Tuffen et al., 2003).

498

499 5.2 Porosity, permeability and micro-structural changes resulting from the densification of
500 high-crystallinity andesitic magma

501

502 *Quantification of key relationships*

503

504 Compiled porosity-permeability datasets from previous studies of various types of volcanic
505 pyroclasts highlight a large amount of scatter that is thought to originate from different
506 decompression rates and degassing, outgassing and deformation processes affecting magma
507 erupted effusively and explosively (e.g. Rust & Cashman 2004; Mueller et al. 2005). Previous
508 authors have provided general relationships between total porosity and permeability for
509 volcanic products that are in the form of power laws based in percolation theory and are
510 constrained empirically (Blower, 2001; Costa, 2006; Klug and Cashman, 1996; Mueller et al.,
511 2005; Saar and Manga, 1999). The topology of the porous network exerts a primary influence
512 on the porosity-permeability relationship (e.g. Bear 1972; Rink 1976; Doyen 1988), for
513 example the geometry and connectivity of pores in compacting granular systems may contrast

markedly with the micro-structures arising from vesiculation in lavas and pyroclasts (Colombier et al., 2017; Heap et al., 2015; Klug and Cashman, 1996; Mueller et al., 2005; Okumura and Sasaki, 2014; Saar and Manga, 1999; Wadsworth et al., 2016; Wright et al., 2009, 2006; Yokoyama and Takeuchi, 2009), as observed in the previous section. In particular, pore sizes, pore throat sizes and tortuosity are expected to exert a large influence on permeability (Degruyter et al., 2010; Saar and Manga, 1999; Zhu and Wong, 1996), as is the extent and anisotropy of heterogeneity (e.g. the variance of the size distributions of pores and throats) (Bernabé et al., 2003; Bernabé and Bruderer, 1998; Farquharson et al., 2016) and the presence of fractures (Heap and Kennedy, 2016; Lamur et al., 2017; Lavallée et al., 2013) whose longevity may vary with healing timescales (Lamur et al., 2019).

As the topology of the porous network in Galeras samples originates from the specific degassing and deformation processes operating during the densification of high-crystallinity andesitic magma, a primary motivation of this study is to establish quantitative relationships that may be used in the future modelling of this process. We fit simple power law regressions by non-linear least squares fitting to our micro-structural datasets in order to characterise these relationships in the well-constrained Galeras system (Fig. 12a–c). We excluded data for the sample of tuffisite material from the fitting procedure as we are primarily interested in the micro-structural changes of the porous network in the host andesite during densification of coherent magma, rather than sintering of granular material. We find that the mean throat area t_a varies with the mean pore volume p_v as: $t_a = 1.058 \times 10^5 \, {p_v}^{0.6}$ (RMSE: 3345 μm^2). The volumetric number density of throats t_n varies with the number density of pores p_n as: $t_n = 2.082 \, {p_n}^{1.331}$ (RMSE: 0.63 mm^{-3}), where we excluded one very dense sample (AB37, shown in black in Fig. 12b) from the fitting procedure as the mean coordination number is 0.4, indicating that the average pore is not connected to any other pores, and this may explain why it forms a clear outlier in the dataset. The mean throat effective radius t_{eff} varies with the mean

effective pore radius p_{eff} as: $t_{eff} = 0.9126\ {p_{eff}}^{0.81}$ (RMSE: 5.3 μm). For this relationship, one very dense sample (GAL5) was excluded from the fitting procedure as the analysis of the micro-tomography data resulted in one pore and no throats after the data cleaning steps. This sample forms a clear outlier in Fig. 10c.

In order to provide a quantitative relationship between connected porosity ϕ_c and permeability k for future modelling of the densification process, we attempted to fit our data using a power law relationship ($k = 5.56 \times 10^{-17}\ \phi_c^{2.96}$, RMSE: 4.02×10^{-13} m^2; shown in Fig. 13). However, we found that the power law relationship did not provide a satisfactory fit to the Galeras data over the 0–15 % range of connected porosity (Fig. 13). Despite a slightly higher error, we find that an exponential relationship provides a more satisfactory fit, especially over the 0–15 % range of connected porosity: $k = 5.46 \times 10^{-17}\ e^{0.38\phi_c}$ (RMSE: 4.52×10^{-13} m^2). For example, for a connected porosity of 7 %, the best-fit power law relationship overestimates permeability by approximately two orders of magnitude (Fig. 13). Our micro-tomography data show that the densification of high-crystallinity porous andesites during plug formation is expressed as decreasing 1) pore volumes, 2) pore throat areas, 3) volumetric number densities of pores, throats and disconnected voids, 4) the variance of pore volumes and pore throat areas, and 5) tortuosity. The best-fit exponential porosity-permeability relationship reflects these micro-structural changes and may be generally appropriate for modelling the densification and plug formation process in high-crystallinity andesitic magmas, as this relationship is distinct from that characterising both vesiculating magmas (Klug and Cashman, 1996; Mueller et al., 2005) and densifying, sintering initially granular systems (e.g. welding ignimbrites (Heap et al., 2015; Wright and Cashman, 2014) and tuffisites (Wadsworth et al., 2016)).

Implications

563

564 The porosity-permeability relationship in ballistic bombs sampling Galeras magma plugs is not
565 consistent with published porosity-permeability data or relationships formulated for explosive
566 products (Fig. 13) (Hill, 1984; Rust and Cashman, 2004; Tait, 2004; Wright et al., 2007, 2006).
567 In contrast, our data agree well with measurements from previous studies on high-crystallinity
568 andesite dome lavas or blocks in block-and-ash flows from Volcán de Colima (Farquharson et
569 al., 2015) and Mount Pelée (Bernard et al., 2007; Jouniaux et al., 2000). Our data are consistent
570 with the notion of a porosity-permeability hysteresis in the context of densifying high-
571 crystallinity magma plugs, as they follow the trend of evolving porosity and permeability in
572 effusive samples thought to reflect an advanced stage of bubble interconnection and collapse
573 (Mueller et al., 2005), rather than explosive samples reflecting various extents of vesiculation
574 and bubble interconnection.

575 Our samples were not erupted effusively, but by examining ballistics that did not vesiculate
576 upon eruptive decompression (Bain et al., 2019), we aim to shed light on the pre-explosive
577 magma conditions prevailing in shallow conduit plugs at Galeras volcano, which are akin to
578 dome lavas erupted effusively at the surface at other andesitic stratovolcanoes. Lava dome
579 emplacement and the congruent development of a shallow conduit plug prior to vulcanian
580 explosions may explain why dome lavas and block-and-ash flow samples follow a similar
581 porosity-permeability trend as Galeras ballistics, as the porous micro-structures in these
582 samples seemingly record the same conduit/dome densification processes. In contrast, other
583 types of effusive products (with different compositions and/or different emplacement
584 mechanisms) may record other processes that affect the porous network (Colombier et al.,
585 2017), e.g. vesiculation or bubble shearing during flow. This generally good agreement
586 supports the idea that the relationships extracted from our data could be used as a first order
587 proxy in modelling the densification process during the emplacement of degassed, highly-

588 crystalline lava domes and plugs. In this context, our data suggest that the decrease in tortuosity
589 (Fig. 10) during densification may be an important process in maintaining permeability to low
590 porosities, permitting plug and dome emplacement and promoting a volcanic style
591 characterised by effusive-explosive transitions.

592 High-temperature experimental compaction studies of natural crystal-poor rhyolite (Ashwell
593 and Kendrick et al., 2015; Gonnermann et al., 2017), crystal-rich rhyolite (Ashwell and
594 Kendrick et al., 2015) and crystal-rich andesite (Kendrick et al., 2013; Lavallée et al., 2013)
595 lavas show contrasting porosity-permeability-strain pathways that emphasise the importance
596 of the nature of the starting material and the strain history. Ashwell and Kendrick et al. (2015)
597 found that crystal-rich (60-70 % of the solid fraction) rhyolite dome samples achieved a
598 compaction limit of 17-19 % porosity, whereas crystal-poor (5% of the solid fraction) rhyolite
599 dome samples likely had a much lower compaction limit that was not achieved in the 60 %
600 strain limit set in their experiments. In that study, crystals hindered the reduction in porosity
601 and permeability during unconfined compaction, whereas natural Galeras samples clearly
602 reached much lower porosities during densification, possibly as a result of the confining
603 pressure in the conduit/dome setting. Gonnermann et al. (2017) observed that the high-
604 temperature, unconfined deformation of crystal-poor pumices resulted in permeability being
605 retained to low values of porosity (<20 %), however our data do not follow the same porosity-
606 permeability reduction pathway (Fig. 13), likely as a result of the difference in deformation
607 conditions (unconfined experimental conditions versus confined natural compaction) and
608 starting material (high-crystallinity andesite versus crystal-poor pumice). In unconfined
609 experiments on high-crystallinity andesites, Kendrick et al. (2013) found that samples
610 deformed to 20 % strain, under low applied stresses to ensure a predominantly viscous response,
611 resulted in a small reduction in porosity and reduction in permeability by two orders of
612 magnitude, whereas those deformed more rapidly were subject to an increase in porosity while

permeability remained unaffected (parallel to compaction). This suggests that confined natural compaction at low strain rates played an important role in allowing the high-crystallinity Galeras samples to densify to very low connected porosities (1.92 %).

The differences in pore and throat properties and tortuosity for low/high permeability pairs of samples described in section 4.3 do not satisfactorily explain the two order of magnitude difference in measured permeability at a given porosity, nor the observed reduced dependence of permeability on confining pressure. We therefore suggest that the low/high permeability pairs in the Galeras sample set may reflect various micro-fracture densities that were not detected in hand sample and were below the resolution of micro-tomography (15–21 μm, see section 3.1), as fractures have been observed to have a dominant effect on permeability in previous studies (Berkowitz, 2002; Heap and Kennedy, 2016; Lamur et al., 2017; Lavallée et al., 2013; Matthäi and Belayneh, 2004). These fractures may have formed either during pre-eruptive deformation as in the study of Kendrick et al. (2013) or during syn-eruptive cooling (e.g. Browning et al., 2016; Lamur et al., 2018) or impact (e.g. Lavallée et al., 2013) of the Galeras bombs.

5.3 Tuffisite

Although a rigorous study of the porosity and permeability of tuffisite veins is beyond the scope of this paper, our micro-tomography data from the sample of tuffisite material analysed here reflects the fundamentally different structure of the porous network compared to the host andesite. In contrast to the host andesite, which exhibits a porous structure arising from the growth, coalescence and collapse of gas bubbles in high-crystallinity magma, tuffisite veins host structures arising from gas-and-ash flow through a fracture followed by settling,

637 compaction and sintering of a granular medium (Kendrick et al., 2016; Tuffen et al., 2003;
638 Wadsworth et al., 2016). Their prevalence in Galeras ballistic samples of all types (Bain et al.,
639 2019) suggests that, despite the retention of permeability during densification of the host
640 andesite, the permeability of localised areas of the magma plugs became insufficient to
641 efficiently dissipate pore pressure, resulting in local fragmentation and the formation of
642 fractures filled with fragmental materials. However, the low tortuosity of porous pathways in
643 this sample suggests that tuffisites represented high permeability pathways within the magma
644 plug with a potentially important role for degassing prior to vulcanian explosions, as shown in
645 previous studies on tuffisite veins (Berlo et al., 2013; Castro et al., 2014, 2012; Kendrick et al.,
646 2016; Kolzenburg et al., 2012; Saubin et al., 2016). This is consistent with the study of Bain et
647 al. (2019) on these ballistic bombs, which suggested that the flux of a S-rich gas phase through
648 these veins served to locally deplete the interstitial melt of the host andesite with respect to
649 H_2O, F and Cl and cause S to become enriched in the melt phase.

650

651 5.4 Implications for eruption dynamics

652

653 *Porous micro-structure and crystal micro-textures*

654

655 Bain et al. (2019) related magma ascent and decompression rates and eruption dynamics at
656 Galeras volcano to systematic variations in plagioclase microlite number density, characteristic
657 size and aspect ratio. Smaller volume explosions in 2004-2008 produced ballistics with crystal
658 micro-textures characterised by small numbers of large, prismatic microlites, whereas larger
659 volume explosions in 2009-2010 produced ballistics with high numbers of small, tabular
660 microlites (Bain et al., 2019). Based on a comparison of these crystal micro-textures with

661 results of decompression experiments by Brugger and Hammer (2010), these changes were
662 determined to have been driven by increasing average decompression rates from 1–10 MPa/h
663 due to increasing magma ascent rates (Bain et al., 2019). Increasing decompression rates
664 resulted in increasing crystal nucleation rates and decreasing crystal growth rates over the
665 course of the eruption sequence, and gave rise to higher plagioclase microlite number densities,
666 smaller characteristic sizes and a change from prismatic to tabular microlites. Here, we
667 compare the plagioclase microlite volumetric number density (N_v), the crystal aspect ratio (S/L,
668 corresponding to the best-fit microlite short axis/long axis) and the characteristic microlite size
669 from the samples in the study of Bain et al. (2019) with the corresponding micro-tomography
670 data collected here to investigate any relationships between the crystal micro-structure and the
671 porous micro-structure (Fig. 14). We find that samples with low N_v, low S/L and large
672 characteristic size (corresponding to crystal micro-textures with small numbers of large,
673 prismatic microlites) typically feature porous networks with higher mean pore volumes and
674 mean throat areas (Fig. 14a–c), as well as higher variance in pore volumes and throat areas.
675 Conversely, samples with high N_v, high S/L and small characteristic size (corresponding to
676 crystal micro-textures with high numbers of small, more tabular microlites) typically feature
677 porous networks with lower mean pore volumes, lower mean throat areas (Fig. 14 a–c), as well
678 as lower variance in pore volumes and throat areas. The breadcrust bomb rind sample features
679 a porous network that is most similar in nature to the porous network in samples with low N_v,
680 low S/L and large characteristic size (Fig. 14). This suggests that andesitic plugs that develop
681 in magma ascending and decompressed at lower average rates (resulting in low N_v, low S/L
682 and large microlite characteristic size) are characterised by a crystal micro-texture that
683 facilitates the retention of the porous network, perhaps as a result of inefficient densification,
684 to produce a comparatively high-permeability plug. This is supported by the observation that
685 the porous network in the breadcrust bomb rind, which records the porous micro-structure in

686 the deepest part of the plug prior to the onset of densification, is most similar to ballistics
687 produced following slow magma ascent. In addition, the presence of lava domes associated
688 with the explosions that produced these ballistic samples (Bain et al., 2019) suggests that pore
689 pressures were effectively dissipated so that lava effusion was possible and repose times
690 between vulcanian explosions became long (hundreds of days). Conversely, plugs that develop
691 in magma ascending and decompressed at higher rates (resulting in high N_v, high S/L and small
692 microlite characteristic size) host porous networks that have undergone significant
693 densification, producing a comparatively low-permeability plug allowing overpressure to build
694 up rapidly, consistent with the short repose times between explosions (tens of days) noted
695 during 2009-2010 (Bain et al., 2019). We suggest that these differences could be the result of
696 a rheological control on the efficiency of densification as a result of the variation in crystal
697 micro-textures. We propose that large, prismatic microlites (low S/L) in these magmatic
698 suspensions are likely to interact more frequently and produce higher bulk magma viscosities
699 than smaller, more tabular microlites (high S/L) (Klein et al., 2018; Mueller et al., 2005), and
700 this could explain the inferred variations in densification efficiency. These rheological
701 variations will be further investigated in future work.

702

703 *Porous micro-structure and groundmass glass volatiles*

704

705 The decrease in connected porosity and permeability as pore volumes, throat areas and the
706 number densities of pores and throats decrease shows that the change in topology of the porous
707 network controls the ability of the densifying magma plug to permit gas flow. However, the
708 timescale over which densification occurs, which may vary significantly due to the rheological
709 differences inferred in the previous section, is also likely to control the ability for a magma
710 plug to degas and outgas. Groundmass glass volatile analyses from Bain et al. (2019) are

711 available for ten of the samples for which micro-tomography data were collected (Fig. 15).
712 These volatile data show that F and Cl follow an overall trend of depletion in the groundmass
713 glass with reducing pore and throat sizes (Fig. 15c–d), despite the occurrence of occasional
714 outliers (e.g. F: 860 ppm, 819ppm and 673 ppm; Cl: 2234 ppm) that may be related to the
715 complex effects of vapour fluxing from depth through degassed magma stored at shallow levels
716 in the conduit (e.g. Bain et al., 2019; Rust et al., 2004; Wright et al., 2007). However, H_2O data
717 reveal an opposite trend (Fig. 15a), with lower groundmass glass water contents generally
718 corresponding to larger pore and throat sizes. In the previous section, we observed that these
719 H_2O-poor samples correspond to magma plugs that densified inefficiently, possibly as a result
720 of rheological controls (e.g. microlite number densities, sizes and shapes) that maintain bubble
721 inter-connections, leading to relatively high-permeability plugs. We suggest that the opposite
722 trend in H_2O and halogen data is related to a trade-off in the rate of densification with respect
723 to the diffusion rate of each species. Rapidly densifying magma plugs (characterised by high
724 N_v, high S/L, small characteristic microlite sizes and low mean pore volumes and mean throat
725 areas) record higher groundmass glass H_2O contents due to the relatively rapid disruption of
726 connected porous pathways and hence rapid destruction of surfaces for diffusive exchange (Fig.
727 16b). More inefficient densification (in magma plugs characterised by low N_v, low S/L, large
728 characteristic microlite sizes and higher mean pore volumes and mean throat areas) results in
729 connected porous pathways remaining open and more extensive degassing of the melt phase
730 with respect to rapidly-diffusing volatile species, such as H_2O (Fig. 16a). In contrast, the slower
731 rates of diffusion of F and Cl (Bai and Koster van Groos, 1994) result in a groundmass glass
732 halogen signature that records magma degassing during emplacement at shallow levels and
733 does not record an effect related to the rate of densification (Fig. 15c–d). In other words, the
734 glass F and Cl contents record progressive degassing during magma emplacement in the
735 shallow conduit, whereas the glass H_2O content records the overprinting process of contrasting

densification rates in magma plugs with different crystal micro-textures and, potentially, rheology (i.e. rapid or slow disruption of porous network connections with apparent viscosity as a limiting factor) as a result of the more rapid diffusion rate. This model is supported by the groundmass glass volatile content of the breadcrust bomb rind, which is sourced from a region in the conduit below the main degassed plug that we focus on in this study. The breadcrust bomb rind contains a similar amount of CO_2, F, Cl and S (Fig. 15b–e) and a similar porous-microstructure (Fig. 14) as the bombs that have undergone the least amount of densification. However, this sample contains a higher water content than all bombs sourced from the degassed region (Fig. 15a), showing that the magma underlying the plugs likely contained a relatively high water concentration before the onset of densification. We therefore propose that, of the volatiles discussed here, water is the only species that diffused rapidly enough to record the differences in plug densification rate prior to vitrification of the groundmass upon ballistic expulsion (Fig. 15-16).

Porous micro-structure beneath the degassed plug

Most breadcrust bombs from Galeras volcano have dense rinds (0–0.5 %), showing that dense magma is stored immediately below the most degassed region of the plugs (100–500 m, Bain et al., 2019). The breadcrust bomb studied here, however, preserves an unusually vesicular rind (~17 %) giving insights into the porous network in magma stored deeper in the conduit (>500 m). The sample taken from the rind of this breadcrust bomb has the largest mean pore volume and mean throat area (Fig. 14), as well as the largest pore volume and throat area variance in the sample set. The porous network in this rind is also the most tortuous and shows a significant anisotropy in tortuosity in three dimensions (Fig. 10). The magma underlying the plugs therefore comprised the highest gas fraction and contained the largest amount of dissolved

761 volatiles in the melt phase, and yet the permeability of this zone may have been limited by the
762 highly contorted paths channelling gas escape.

763 Bain et al. (2019) inferred higher degassing-driven effective undercooling in magma below the
764 most degassed part of the plug in order to explain consistently higher microlite N_v in deeper-
765 sourced breadcrust bombs relative to dense and scoriaceous bombs. The large mean pore
766 volumes, mean throat areas and high variance in the scales of the porous micro-structures in
767 this breadcrust bomb rind support the idea of a larger degassing increment in the area below
768 the plugs, as gas flow localisation through preferred pathways is expected to occur in highly
769 heterogeneous porous media (Bernabé and Bruderer, 1998; Laumonier et al., 2011; Lavallée et
770 al., 2013; Wright and Weinberg, 2009) and may have initially promoted rapid outgassing.
771 However, the propensity for gas flow localisation may eventually be countered by the high
772 tortuosity of the connected pathways during ongoing degassing.

773 These observations support the hypothesis from Bain et al. (2019) that the region of the magma
774 column emplaced in the shallow conduit where significant overpressure is likely to have
775 developed is located below the degassed, low-permeability plugs, as previously suggested in
776 the studies of Clarke et al. (2007), Giachetti et al., (2010), Hammer et al. (1999); Sparks (1997),
777 and Wright et al. (2007). We therefore propose the following model for vulcanian explosions
778 as Galeras volcano. Prior to individual vulcanian explosions, pore pressures within the
779 viscously compacting andesitic magma plug emplaced in the shallow conduit (<500 m) were
780 decreasing, as we have shown here that permeability was largely retained within the magma
781 plugs and densification could occur without the development of large-scale pore overpressure.
782 We propose that only small-scale, localised pore overpressure developed within the plugs,
783 evidenced by the occurrence of tuffisite veins. In contrast, the high variance in pore sizes and
784 throat areas in the region below the degassed plugs, as evinced by the porous network in the
785 breadcrust bomb rind, may have enhanced the possibility for pore overpressure development

786 by forcing rapidly moving gas to stall in pores with smaller throats or to rapidly infiltrate
787 smaller pores through large throats during gas flux. The results of this study suggest that the
788 porous network in this deeper region with a highly tortuous and anisotropic porous network
789 (Fig. 1) that was not preserved as ballistics but pulverised into ash is likely to have exhibited
790 the most favourable conditions for large-scale pore overpressure during gas fluxing, resulting
791 in the fragmentation and explosive eruption of the magma plugs. Based on the data presented
792 in this paper, we propose that the timescale for this large-scale overpressure development may
793 have been controlled by the permeability of the most degassed portion of the plug, which was
794 dependent on the crystal micro-textures dictated by changing decompression rates, which may
795 have exerted a rheological control on densification rate.

796

797 **6. Conclusions**

798

799 We have combined an experimental determination of the connected porosity and gas
800 permeability of ballistic bombs produced by the 2004-2010 sequence of vulcanian explosions
801 at Galeras volcano, Colombia, with micro-tomographic reconstructions of the porous micro-
802 structures to illustrate the changes in the porous network that occur as a result of the
803 densification of high-crystallinity andesitic magma plugs. Densification results in the reduction
804 of mean pore volumes and mean throat areas, as well as a reduction in the volumetric number
805 density of pores and throats. We observe a relative loss of throats compared to pores and a
806 decline of disconnected voids with reducing porosity, suggesting progressive pore closure
807 and/or coalescence of isolated pores to the connected network. These micro-structural changes
808 produced a reduction in tortuosity of the permeable pathways during magma densification,
809 enabling the development of a plug without the large-scale development of gas overpressure

owing to the retention of permeability to low levels of connected porosity. In contrast, magma residing at deeper levels below densifying plugs is characterised by large pore volumes and pore throat areas, but the high variance of these properties and the high tortuosity and anisotropy of the porous network suggest that pore overpressure may be more likely to develop at these deeper levels in the conduit, providing the driving force for vulcanian explosions. In combination with previously-published crystal micro-texture and groundmass glass volatile data, the porous micro-structure data presented here argues for a plug formation model where variations in densification rate and final permeability are controlled by variations in crystal micro-textures. The extent of densification, plug permeability and plug degassing may therefore be ultimately controlled by magma decompression and ascent rates, which control the variations in crystal micro-textures that modulate magma rheology and densification rate. Building understanding of the links between magma ascent rates, crystal micro-textures, bulk magma rheology and densification processes may therefore provide important insights into vulcanian eruption explosivity.

Acknowledgements

This work was funded by a Natural Environment Research Council Doctoral Training Partnership grant [NE/L002558/1] to A. Bain. Y. Lavallée, A. Lamur and the Experimental Volcanology and Geothermal Research Laboratory at the University of Liverpool were supported by a starting grant of the European Research Council (ERC) on Strain Localisation in Magma [SLiM; no. 306488]. J. E. Kendrick was supported by an Early Career Fellowship of the Leverhulme Trust. A. Bain thanks Wim Degruyter for kindly sharing the 3DMA-Rock code and providing advice on implementation, and Rebekah Harries for helpful discussions. The authors thank two anonymous reviewers for their helpful and constructive comments, and Heidy Mader for editorial handling.

Competing Interests Statement

The authors declare no competing interests.

References

Ashwell, P.A., Kendrick, J.E., Lavallée, Y., Kennedy, B.M., Hess, K.U., Von Aulock, F.W., Wadsworth, F.B., Vasseur, J., Dingwell, D.B., 2015. Permeability of compacting porous lavas. J. Geophys. Res. B Solid Earth 120, 1605–1622. https://doi.org/10.1002/2014JB011519

Bai, T.B., Koster van Groos, A.F., 1994. Diffusion of chlorine in granitic melts. Geochim. Cosmochim. Acta 58, 113–123. https://doi.org/10.1016/0016-7037(94)90450-2

Bain, A.A., Calder, E.S., Cortés, J.A., Cortés, G.P., Loughlin, S., 2019. Textural and geochemical constraints on andesitic plug emplacement prior to the 2004-2010 vulcanian explosions at Galeras volcano, Colombia. Bull. Volcanol. 81, 1.

Bear, J., 1972. Dynamics of fluids in porous media. American Elsevier Publishing Co. Inc., New York.

Berkowitz, B., 2002. Characterizing flow and transport in fractured geological media: A review. Adv. Water Resour. 25, 861–884. https://doi.org/10.1016/S0309-1708(02)00042-8

Berlo, K., Tuffen, H., Smith, V.C., Castro, J.M., Pyle, D.M., Mather, T.A., Geraki, K., 2013. Element variations in rhyolitic magma resulting from gas transport. Geochim. Cosmochim. Acta 121, 436–451. https://doi.org/10.1016/j.gca.2013.07.032

858 Bernabé, Y., Bruderer, C., 1998. Effect of the variance of pore size distribution on the
859 transport properties of heterogeneous networks. J. Geophys. Res. Solid Earth 103, 513–
860 525. https://doi.org/10.1029/97JB02486

861 Bernabé, Y., Mok, U., Evans, B., 2003. Permeability-porosity relationships in rocks subjected
862 to various evolution processes. Pure Appl. Geophys. 160, 937–960.
863 https://doi.org/10.1007/PL00012574

864 Bernard, M.L., Zamora, M., Géraud, Y., Boudon, G., 2007. Transport properties of
865 pyroclastic rocks from Montagne Pelée volcano (Martinique, Lesser Antilles). J.
866 Geophys. Res. Solid Earth 112, 1–16. https://doi.org/10.1029/2006JB004385

867 Blower, J., 2001. Factors controlling permeability-porosity relationships in magma. Bull.
868 Volcanol. 63, 497–504. https://doi.org/10.1007/s004450100172

869 Browning, J., Meredith, P., Gudmundsson, A., 2016. Cooling-dominated cracking in
870 thermally stressed volcanic rocks. Geophys. Res. Lett. 43, 8417–8425.
871 https://doi.org/10.1002/2016GL070532

872 Brugger, C.R., Hammer, J.E., 2010. Crystallization kinetics in continuous decompression
873 experiments: Implications for interpreting natural magma ascent processes. J. Petrol. 51,
874 1941–1965. https://doi.org/10.1093/petrology/egq044

875 Burgisser, A., Chevalier, L., Gardner, J.E., Castro, J.M., 2017. The percolation threshold and
876 permeability evolution of ascending magmas. Earth Planet. Sci. Lett. 470, 37–47.
877 https://doi.org/10.1016/j.epsl.2017.04.023

878 Cashman, K., Blundy, J., 2000. Degassing and crystallization of ascending andesite and
879 dacite. Philos. Trans. R. Soc. London A Math. Phys. Eng. Sci. 358, 1487–1513.

880 Cassidy, M., Manga, M., Cashman, K., Bachmann, O., 2018. Controls on explosive-effusive
881 volcanic eruption styles. Nat. Commun. 9, 2839. https://doi.org/10.1038/s41467-018-

882 05293-3

883 Castro, J.M., Bindeman, I.N., Tuffen, H., Ian Schipper, C., 2014. Explosive origin of silicic
884 lava: Textural and delta-H20 evidence for pyroclastic degassing during rhyolite effusion.
885 Earth Planet. Sci. Lett. 405, 52–61. https://doi.org/10.1016/j.epsl.2014.08.012

886 Castro, J.M., Cordonnier, B., Tuffen, H., Tobin, M.J., Puskar, L., Martin, M.C., Bechtel,
887 H.A., 2012. The role of melt-fracture degassing in defusing explosive rhyolite eruptions
888 at volcan Chaitén. Earth Planet. Sci. Lett. 333–334, 63–69.
889 https://doi.org/10.1016/j.epsl.2012.04.024

890 Clarke, A.B., 2013. Unsteady explosive activity: vulcanian eruptions, in: Fagents, S.A.,
891 Gregg, T.K.P., Lopes, R.M.C. (Eds.), Modeling Volcanic Processes: The Physics and
892 Mathematics of Volcanism. Cambridge University Press.

893 Clarke, A.B., Stephens, S., Teasdale, R., Sparks, R.S.J., Diller, K., 2007. Petrologic
894 constraints on the decompression history of magma prior to Vulcanian explosions at the
895 Soufrière Hills volcano, Montserrat. J. Volcanol. Geotherm. Res. 161, 261–274.
896 https://doi.org/10.1016/j.jvolgeores.2006.11.007

897 Coats, R., Kendrick, J.E., Wallace, P.A., Miwa, T., Hornby, A.J., Ashworth, J.D.,
898 Matsushima, T., Lavallée, Y., 2018. Failure criteria for porous dome rocks and lavas: a
899 study of Mt. Unzen, Japan. Solid Earth Discuss. https://doi.org/10.5194/se-2018-19

900 Colombier, M., Wadsworth, F.B., Gurioli, L., Scheu, B., Kueppers, U., Di Muro, A.,
901 Dingwell, D.B., 2017. The evolution of pore connectivity in volcanic rocks. Earth
902 Planet. Sci. Lett. 462, 99–109. https://doi.org/10.1016/j.epsl.2017.01.011

903 Costa, A., 2006. Permeability-porosity relationship: A reexamination of the Kozeny-Carman
904 equation based on a fractal pore-space geometry assumption. Geophys. Res. Lett. 33, 1–
905 5. https://doi.org/10.1029/2005GL025134

906 Darcy, H., 1857. Recherches expérimentales relatives au mouvement de l'eau dans les
907 tuyaux. Mallet-Bachelier.

908 Darcy, H., 1856. Les fontaines publiques de la ville de Dijon: exposition et application...
909 Victor Dalmont.

910 Degruyter, W., Bachmann, O., Burgisser, A., 2010. Controls on magma permeability in the
911 volcanic conduit during the climactic phase of the Kos Plateau Tuff eruption (Aegean
912 Arc). Bull. Volcanol. 72, 63–74. https://doi.org/10.1007/s00445-009-0302-x

913 Dierick, M., Masschaele, B., Van Hoorebeke, L., 2004. Octopus, a fast and user-friendly
914 tomographic reconstruction package developed in LabView. Meas. Sci. Technol. 15,
915 1366–1370. https://doi.org/10.1088/0957-0233/15/7/020

916 Dingwell, D., 1996. Volcanic dilemma: flow or blow? Science (80-.). 273, 1054–1055.

917 Doyen, P.M., 1988. Permeability, conductivity, and pore geometry of sandstone. J. Geophys.
918 Res. 93, 7729–7740. https://doi.org/10.1029/JB093iB07p07729

919 Eichelberger, J., Carrigan, C., Westrich, H., Price, R., 1986. Non-explosive silicic volcanism.
920 Nature 323, 598–602.

921 Farquharson, J., Heap, M.J., Varley, N.R., Baud, P., Reuschle, T., 2015. Permeability and
922 porosity relationships of edifice-forming andesites: A combined field and laboratory
923 study. J. Volcanol. Geotherm. Res. 297, 52–68.
924 https://doi.org/10.1016/j.jvolgeores.2015.03.016

925 Farquharson, J.I., Heap, M.J., Lavallée, Y., Varley, N.R., Baud, P., 2016. Evidence for the
926 development of permeability anisotropy in lava domes and volcanic conduits. J.
927 Volcanol. Geotherm. Res. 323, 163–185.
928 https://doi.org/10.1016/j.jvolgeores.2016.05.007

929 Giachetti, T., Druitt, T.H., Burgisser, A., Arbaret, L., Galven, C., 2010. Bubble nucleation,
930 growth and coalescence during the 1997 Vulcanian explosions of Soufrière Hills
931 Volcano, Montserrat. J. Volcanol. Geotherm. Res. 193, 215–231.
932 https://doi.org/10.1016/j.jvolgeores.2010.04.001

933 Gonnermann, H.M., Giachetti, T., Fliedner, C., Nguyen, C.T., Houghton, B.F., Crozier, J.A.,
934 Carey, R.J., 2017. Permeability During Magma Expansion and Compaction. J. Geophys.
935 Res. Solid Earth 122, 9825–9848. https://doi.org/10.1002/2017JB014783

936 Hammer, J.E., Cashman, K.V., Voight, B., 2000. Magmatic processes revealed by textural
937 and compositional trends in Merapi dome lavas. J. Volcanol. Geotherm. Res. 100, 165–
938 192. https://doi.org/10.1016/S0377-0273(00)00136-0

939 Hammer, J.E., Cashman, K. V., Hoblitt, R.P., Newman, S., 1999. Degassing and microlite
940 crystallization during pre-climactic events of the 1991 eruption of Mt. Pinatubo,
941 Philippines. Bull. Volcanol. 60, 355–380. https://doi.org/10.1007/s004450050238

942 Heap, M.J., Farquharson, J.I., Wadsworth, F.B., Kolzenburg, S., Russell, J.K., 2015.
943 Timescales for permeability reduction and strength recovery in densifying magma. Earth
944 Planet. Sci. Lett. 429, 223–233. https://doi.org/10.1016/j.epsl.2015.07.053

945 Heap, M.J., Kennedy, B., 2016. Exploring the Scale-Dependent permeability of fractured
946 andesite. Earth Planet. Sci. Lett. 447, 956–963.
947 https://doi.org/10.1017/CBO9781107415324.004

948 Heap, M.J., Reuschlé, T., Farquharson, J.I., Baud, P., 2018. Permeability of volcanic rocks to
949 gas and water. J. Volcanol. Geotherm. Res. 354, 29–38.
950 https://doi.org/10.1016/j.jvolgeores.2018.02.002

951 Heap, M.J., Violay, M., Wadsworth, F.B., Vasseur, J., 2017. From rock to magma and back
952 again: The evolution of temperature and deformation mechanism in conduit margin

zones. Earth Planet. Sci. Lett. 463, 92–100. https://doi.org/10.1016/j.epsl.2017.01.021

Hill, B.E., 1984. Petrology of the Bend pumice and Tumalo tuff, a Pleistocene Cascade eruption involving magma mixing.

Hoblitt, R.P., Harmon, R.S., 1993. Bimodal Density Distribution of Cryptodome Dacite from the 1980 Eruption of Mount St. Helens, Washington. Bull. Volcanol. 55, 421–437. https://doi.org/10.1007/BF00302002

Jouniaux, L., Bernard, M.-L., Zamora, M., Pozzi, J.-P., 2000. Streaming potential in volcanic rocks from Mount Peleé. J. Geophys. Res. 105, 8391–8401. https://doi.org/10.1029/1999jb900435

Kendrick, J.E., Lavallée, Y., Hess, K.U., Heap, M.J., Gaunt, H.E., Meredith, P.G., Dingwell, D.B., 2013. Tracking the permeable porous network during strain-dependent magmatic flow. J. Volcanol. Geotherm. Res. 260, 117–126. https://doi.org/10.1016/j.jvolgeores.2013.05.012

Kendrick, J.E., Lavallée, Y., Varley, N.R., Wadsworth, F.B., Lamb, O.D., Vasseur, J., 2016. Blowing Off Steam: Tuffisite Formation As a Regulator for Lava Dome Eruptions. Front. Earth Sci. 4, 1–15. https://doi.org/10.3389/feart.2016.00041

Kennedy, B.M., Wadsworth, F.B., Vasseur, J., Ian Schipper, C., Mark Jellinek, A., von Aulock, F.W., Hess, K.-U., Kelly Russell, J., Lavallée, Y., Nichols, A.R.L., Dingwell, D.B., 2016. Surface tension driven processes densify and retain permeability in magma and lava. Earth Planet. Sci. Lett. 433, 116–124. https://doi.org/10.1016/j.epsl.2015.10.031

Klein, J., Mueller, S.P., Helo, C., Gurioli, L., Castro, J.M., 2018. An expanded model and application of the combined effect of crystal-size distribution and crystal shape on the relative viscosity of magmas. J. Volcanol. Geotherm. Res. 357, 128–133.

https://doi.org/10.1016/j.jvolgeores.2018.04.018

Klinkenberg, L., 1941. The permeability of porous media to liquids and gases, in: Drilling and Production Practice.

Klug, C., Cashman, K. V., 1996. Permeability development in vesiculating magmas: implications for fragmentation. Bull. Volcanol. 58, 87–100. https://doi.org/10.1007/s004450050128

Kolzenburg, S., Heap, M.J., Lavallée, Y., Russell, J.K., Meredith, P.G., Dingwell, D.B., 2012. Strength and permeability recovery of tuffisite-bearing andesite. Solid Earth 3, 191–198. https://doi.org/10.5194/se-3-191-2012

Kushnir, A.R.L., Martel, C., Champallier, R., Wadsworth, F.B., 2017. Permeability Evolution in Variably Glassy Basaltic Andesites Measured Under Magmatic Conditions. Geophys. Res. Lett. 44, 10,262-10,271. https://doi.org/10.1002/2017GL074042

Lamur, A., Kendrick, J.E., Eggertsson, G.H., Wall, R.J., Ashworth, J.D., Lavallée, Y., 2017. The permeability of fractured rocks in pressurised volcanic and geothermal systems. Sci. Rep. 7, 1–9. https://doi.org/10.1038/s41598-017-05460-4

Lamur, A., Kendrick, J.E., Wadsworth, F.B., Lavallée, Y., 2019. Fracture healing and strength recovery in magmatic liquids. Geology 47, 1–4. https://doi.org/10.1130/G45512.1

Lamur, A., Lavallée, Y., Iddon, F.E., Hornby, A.J., Kendrick, J.E., Von Aulock, F.W., Wadsworth, F.B., 2018. Disclosing the temperature of columnar jointing in lavas. Nat. Commun. 9. https://doi.org/10.1038/s41467-018-03842-4

Laumonier, M., Arbaret, L., Burgisser, A., Champallier, R., 2011. Porosity redistribution enhanced by strain localization in crystal-rich magmas. Geology 39, 715–718. https://doi.org/10.1130/G31803.1

1001 Lavallée, Y., Benson, P.M., Heap, M.J., Hess, K.U., Flaws, A., Schillinger, B., Meredith,
1002 P.G., Dingwell, D.B., 2013. Reconstructing magma failure and the degassing network of
1003 domebuilding eruptions. Geology 41, 515–518. https://doi.org/10.1130/G33948.1

1004 Lavallée, Y., Varley, N.R., Alatorre-Ibargüengoitia, M.A., Hess, K.U., Kueppers, U.,
1005 Mueller, S., Richard, D., Scheu, B., Spieler, O., Dingwell, D.B., 2012. Magmatic
1006 architecture of dome-building eruptions at Volcán de Colima, Mexico. Bull. Volcanol.
1007 74, 249–260. https://doi.org/10.1007/s00445-011-0518-4

1008 Lee, T.-C., Kashyap, R.L., Chu, C.-N., 1994. Building skeleton models via 3-D medial
1009 surface/axis thinning algorithms. CVGIP Graph. Model. image Process. 56, 462–478.

1010 Lindoo, A., Larsen, J.F., Cashman, K. V., Oppenheimer, J., 2017. Crystal controls on
1011 permeability development and degassing in basaltic andesite magma. Geology 45, 831–
1012 834. https://doi.org/10.1130/G39157.1

1013 Lindquist, W.B., Venkatarangan, A., 1999. Investigating 3D geometry of porous media from
1014 high resolution images. Phys. Chem. Earth, Part A Solid Earth Geod. 24, 593–599.
1015 https://doi.org/10.1016/S1464-1895(99)00085-X

1016 Matthäi, S.K., Belayneh, M., 2004. Fluid flow partitioning between fractures and a permeable
1017 rock matrix. Geophys. Res. Lett. 31, 1–5. https://doi.org/10.1029/2003GL019027

1018 Michaut, C., Bercovici, D., Sparks, R.S.J., 2009. Ascent and compaction of gas rich magma
1019 and the effects of hysteretic permeability. Earth Planet. Sci. Lett. 282, 258–267.
1020 https://doi.org/10.1016/j.epsl.2009.03.026

1021 Mueller, S., Melnik, O., Spieler, O., Scheu, B., Dingwell, D.B., 2005. Permeability and
1022 degassing of dome lavas undergoing rapid decompression: An experimental
1023 determination. Bull. Volcanol. 67, 526–538. https://doi.org/10.1007/s00445-004-0392-4

1024 Oh, W., Lindquist, B.W., 1999. Image thresholding by indicator kriging. IEEE Trans. Pattern

1025 Anal. Mach. Intell. 21, 590–602. https://doi.org/10.1109/34.777370

1026 Okumura, S., Nakamura, M., Takeuchi, S., Tsuchiyama, A., Nakano, T., Uesugi, K., 2009.
1027 Magma deformation may induce non-explosive volcanism via degassing through bubble
1028 networks. Earth Planet. Sci. Lett. 281, 267–274.
1029 https://doi.org/10.1016/j.epsl.2009.02.036

1030 Okumura, S., Nakamura, M., Uesugi, K., Nakano, T., Fujioka, T., 2013. Coupled effect of
1031 magma degassing and rheology on silicic volcanism. Earth Planet. Sci. Lett. 362, 163–
1032 170. https://doi.org/10.1016/j.epsl.2012.11.056

1033 Okumura, S., Sasaki, O., 2014. Permeability reduction of fractured rhyolite in volcanic
1034 conduits and its control on eruption cyclicity. Geology 42, 843–846.
1035 https://doi.org/10.1130/G35855.1

1036 Preece, K., Gertisser, R., Barclay, J., Charbonnier, S.J., Komorowski, J.-C., Herd, R.A., 2016.
1037 Transitions between explosive and effusive phases during the cataclysmic 2010 eruption
1038 of Merapi volcano, Java, Indonesia. Bull. Volcanol. 78, 54.
1039 https://doi.org/10.1007/s00445-016-1046-z

1040 Rink, B.Y.M., 1976. Pore Structure and Physical Properties of Porous Sedimentary Rocks
1041 114.

1042 Rust, a. C., Cashman, K.V., Wallace, P.J., 2004. Magma degassing buffered by vapor flow
1043 through brecciated conduit margins. Geology 32, 349. https://doi.org/10.1130/G20388.2

1044 Rust, A.C., Cashman, K.V., 2004. Permeability of vesicular silicic magma: inertial and
1045 hysteresis effects. Earth Planet. Sci. Lett. 228, 93–107.
1046 https://doi.org/10.1016/j.epsl.2004.09.025

1047 Saar, M.O., Manga, M., 1999. Permeability-porosity relationships in vesicular basalts.
1048 Geophys. Res. Lett. 26, 111–114.

1049 Sato, H., Fujii, T., Nakada, S., 1992. Crumbling of dacite dome lava and generation of
1050 pyroclastic flows at Unzen volcano. Nature 360, 664–666.

1051 Saubin, E., Tuffen, H., Gurioli, L., Owen, J., Castro, J.M., Berlo, K., McGowan, E.M.,
1052 Schipper, C.I., Wehbe, K., 2016. Conduit Dynamics in Transitional Rhyolitic Activity
1053 Recorded by Tuffisite Vein Textures from the 2008–2009 Chaitén Eruption. Front. Earth
1054 Sci. 4. https://doi.org/10.3389/feart.2016.00059

1055 Schneider, C.A., Rasband, W.S., Eliceiri, K.W., 2012. NIH Image to ImageJ: 25 years of
1056 image analysis. Nat. Methods 9, 671–675. https://doi.org/10.1038/nmeth.2089

1057 Silver, L.A., Ihinger, P.D., Stolper, E., 1990. The influence of bulk composition on the
1058 speciation of water in silicate glasses. Contrib. to Mineral. Petrol. 104, 142–162.
1059 https://doi.org/10.1007/BF00306439

1060 Sparks, R.S.J., 1997. Causes and consequences of pressurisation in lava dome eruptions.
1061 Earth Planet. Sci. Lett. 150, 177–189. https://doi.org/10.1016/S0012-821X(97)00109-X

1062 Stix, J., Calvache, M., Fischer, T., Gómez, D., 1993. A model of degassing at Galeras
1063 Volcano, Colombia, 1988-1993. Geology 21, 963–967. https://doi.org/10.1130/0091-
1064 7613(1993)021<0963

1065 Stix, J., Torres, R.C., Medina, L.N., Cortés, G.P., Raigosa, J.A., Gómez, D., Castonguay, R.,
1066 1997. A model of vulcanian eruptions at Galeras volcano, Colombia. J. Volcanol.
1067 Geotherm. Res. 77, 285–303.

1068 Tait, M.A., 2004. Dynamics of a large volume plinian eruption: dispersal of the late Miocene
1069 Corte Blanco tuff, Ramadas Volcanic Centre, Andes Mountains, Salta, Argentina.
1070 Monash University.

1071 Takeuchi, S., Nakashima, S., Tomiya, A., Shinohara, H., 2005. Experimental constraints on
1072 the low gas permeability of vesicular magma during decompression. Geophys. Res. Lett.

1073 32, 1–5. https://doi.org/10.1029/2005GL022491

1074 Tuffen, H., Dingwell, D.B., Pinkerton, H., 2003. Repeated fracture and healing of silicic
1075 magma generate flow banding and earthquakes? Geology 31, 1089–1092.
1076 https://doi.org/10.1130/G19777.1

1077 Voight, B., 1999. Magma Flow Instability and Cyclic Activity at Soufriere Hills Volcano,
1078 Montserrat, British West Indies. Science (80-.). 283, 1138–1142.

1079 Wadsworth, F.B., Vasseur, J., Llewellin, E.W., Dobson, K.J., Colombier, M., Von Aulock,
1080 F.W., Fife, J.L., Wiesmaier, S., Hess, K.U., Scheu, B., Lavallée, Y., Dingwell, D.B.,
1081 2017. Topological inversions in coalescing granular media control fluid-flow regimes.
1082 Phys. Rev. E 96, 1–6. https://doi.org/10.1103/PhysRevE.96.033113

1083 Wadsworth, F.B., Vasseur, J., Scheu, B., Kendrick, J.E., Lavallée, Y., Dingwell, D.B., 2016.
1084 Universal scaling of fluid permeability during volcanic welding and sediment
1085 diagenesis. Geology 44, 219–222. https://doi.org/10.1130/G37559.1

1086 Whitaker, S., 1996. The Forchheimer equation: A theoretical development. Transp. Porous
1087 Media 25, 27–61. https://doi.org/10.1007/BF00141261

1088 Wright, H.M., Cashman, K. V., 2014. Compaction and gas loss in welded pyroclastic
1089 deposits as revealed by porosity, permeability, and electrical conductivity measurements
1090 of the Shevlin Park Tuff. Bull. Geol. Soc. Am. 126, 234–247.
1091 https://doi.org/10.1130/B30668.1

1092 Wright, H.M.N., Cashman, K. V., Gottesfeld, E.H., Roberts, J.J., 2009. Pore structure of
1093 volcanic clasts: Measurements of permeability and electrical conductivity. Earth Planet.
1094 Sci. Lett. 280, 93–104. https://doi.org/10.1016/j.epsl.2009.01.023

1095 Wright, H.M.N., Cashman, K. V, Rosi, M., Cioni, R., 2007. Breadcrust bombs as indicators
1096 of Vulcanian eruption dynamics at Guagua Pichincha volcano, Ecuador. Bull. Volcanol.

69, 281–300.

Wright, H.M.N., Roberts, J.J., Cashman, K. V., 2006. Permeability of anisotropic tube pumice: Model calculations and measurements. Geophys. Res. Lett. 33. https://doi.org/10.1029/2006GL027224

Wright, H.M.N., Weinberg, R.F., 2009. Strain localization in vesicular magma: Implications for rheology and fragmentation. Geology 37, 1023–1026. https://doi.org/10.1130/G30199A.1

Yokoyama, T., Takeuchi, S., 2009. Porosimetry of vesicular volcanic products by a water-expulsion method and the relationship of pore characteristics to permeability. J. Geophys. Res. Solid Earth 114. https://doi.org/10.1029/2008JB005758

Zhu, W., Wong, F., 1996. Damage and Tortuosity 23, 3099–3102.

Figures :

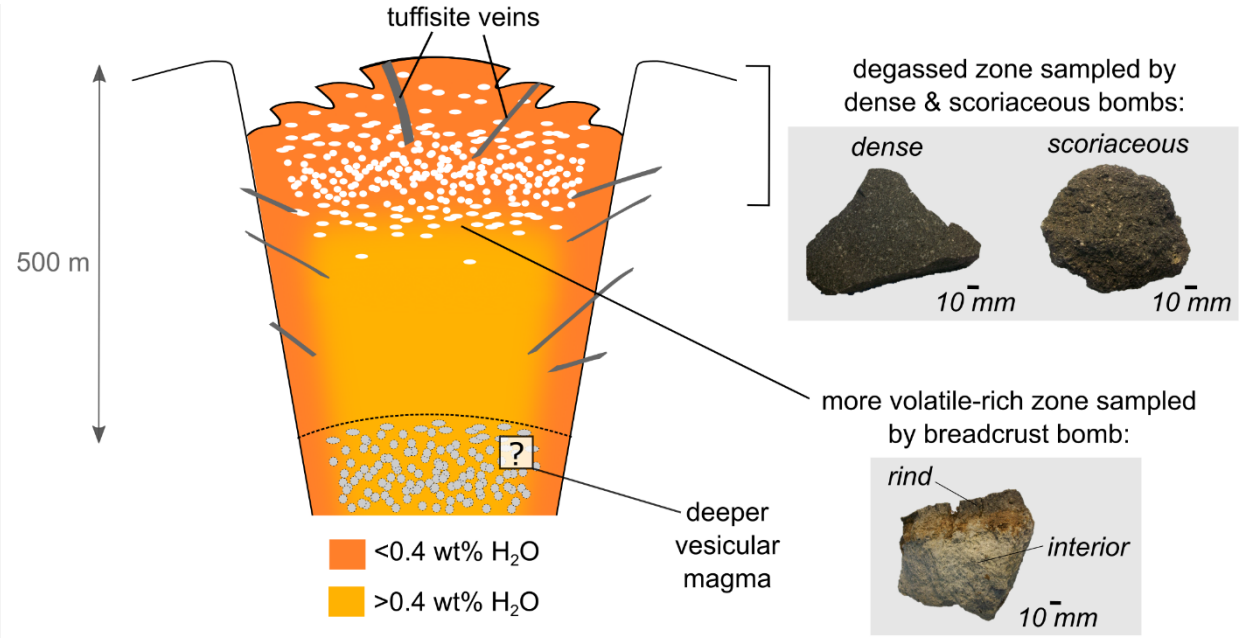

Fig. 1: Structure of the average andesitic magma plug at Galeras volcano, modified from Bain et al. (2019), showing the properties of the source areas for the three different bomb types produced in the 2004-2010 vulcanian explosions. Dense and scoriaceous bombs were typically sourced from no more than 100 m depth in the conduit. The breadcrust bomb shown here is a fragment displaying the highly vesicular bomb interior resulting from syn-eruptive vesiculation and the dense exterior rind representative of the pre-eruptive magma properties. Dense and scoriaceous bombs did not experience syn-eruptive vesiculation and preserve the pre-eruptive magma properties. Also shown is a hypothetical deeper zone of vesicular magma (>500 m) that may represent the region where pore overpressure increased sufficiently to drive vulcanian explosions (Bain et al. 2019).

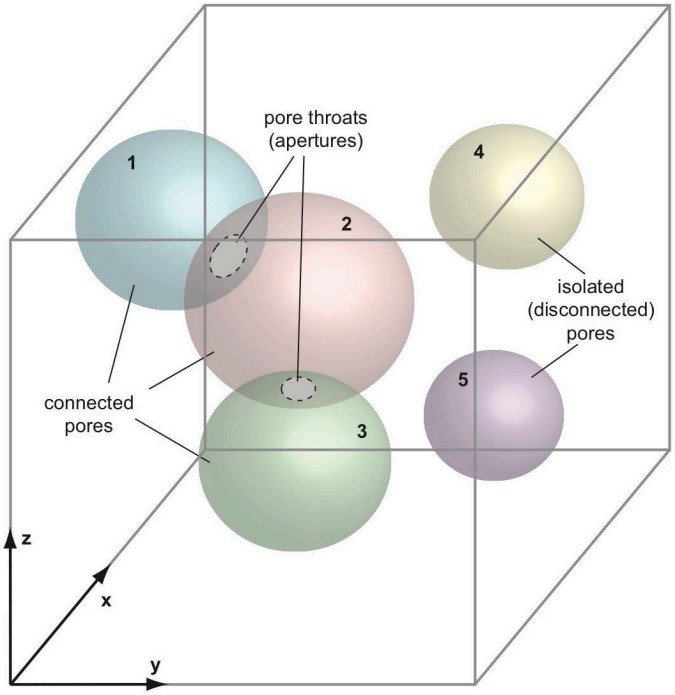

Fig. 2: Simplified illustration of the porous network analysed by micro-tomography (pores are not spherical in real samples, see Fig. 4 & 5). This example volume contains three connected pores (1, 2 & 3) and two pore throats, as well as two disconnected pores or voids (4 & 5). Pores 1 and 3 have a coordination number of 1 and pore 2 has a coordination number of 2. Connected and isolated pores were quantified as separate populations, giving volumetric number densities of connected pores and disconnected voids, as well as a volumetric number density of pore throats. The volumes of connected pores and isolated pores were also measured, as well as throat surface areas. Permeability was measured parallel to the z direction (see frame of reference).

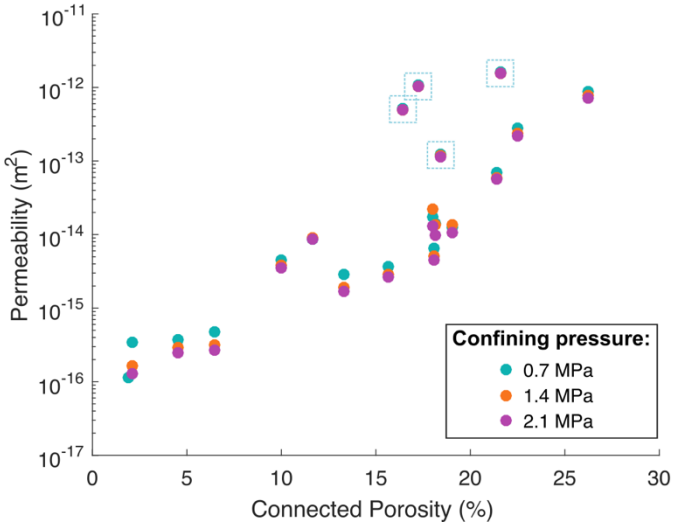

1145

1146 **Fig. 3:** Gas permeability varies from 1.13×10^{-16} – 1.63×10^{-12} m^2 over the measured range
1147 of connected porosity (1.9-26.3 %) and the range of applied confining pressures (0.7-2.1
1148 MPa). Propagated errors for connected porosity and permeability measurements are smaller
1149 than the symbol size, see section 3.2. Permeability is lower in samples with lower connected
1150 porosity and permeability for each sample is lower at higher confining pressures. Dashed
1151 boxes indicate samples with higher permeability (GAL6, GAL8, GAL13, GAL19) than other
1152 samples with similar connected porosity, see section 4.1 and Table 1.

1153

1154

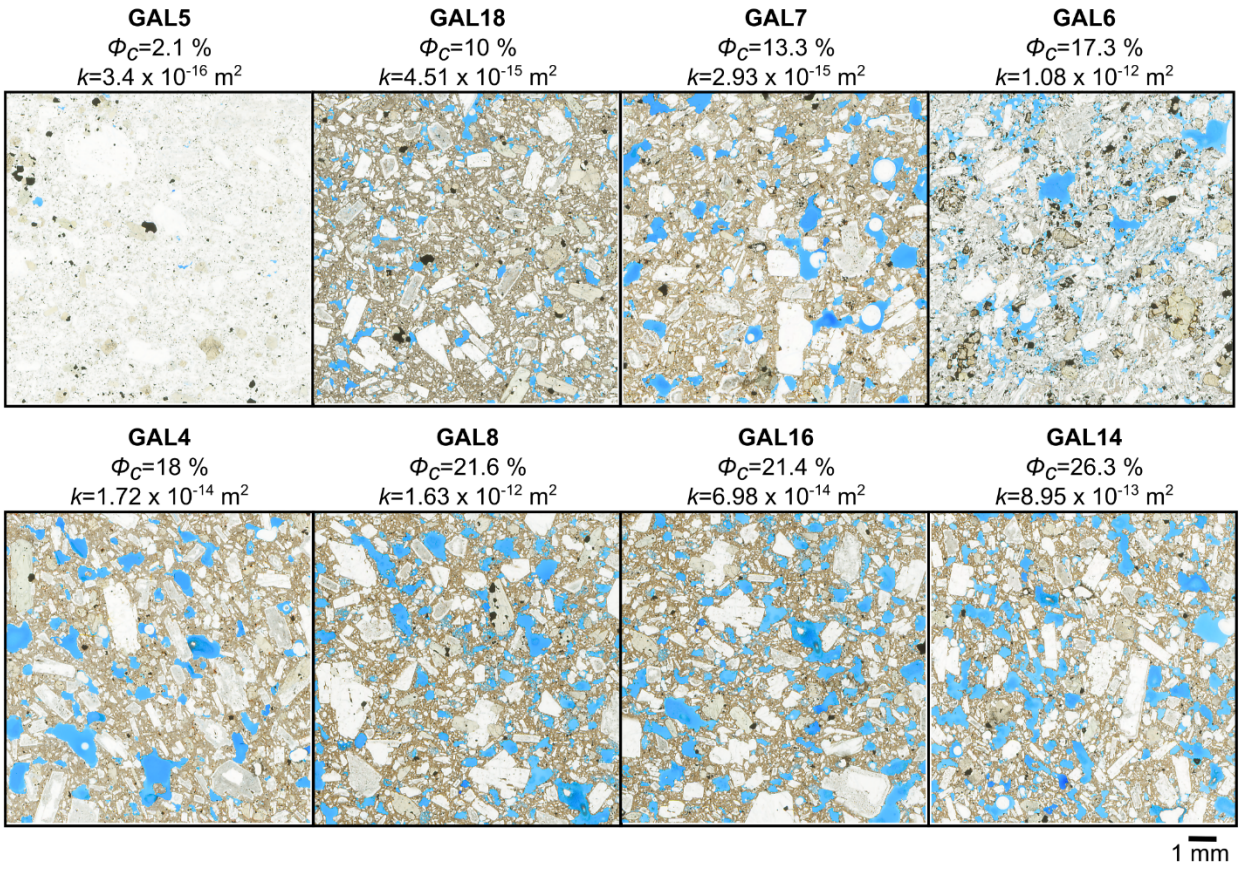

1155

1156 **Fig. 4:** Scanned images of sample thin sections with increasing connected porosities ϕ_c.

1157 Permeability, k, measured at 0.7 MPa confining pressure is also indicated. All samples are

1158 porphyritic andesite bombs. Voids are shown in blue epoxy resin with occasional rounded

1159 white air bubbles.

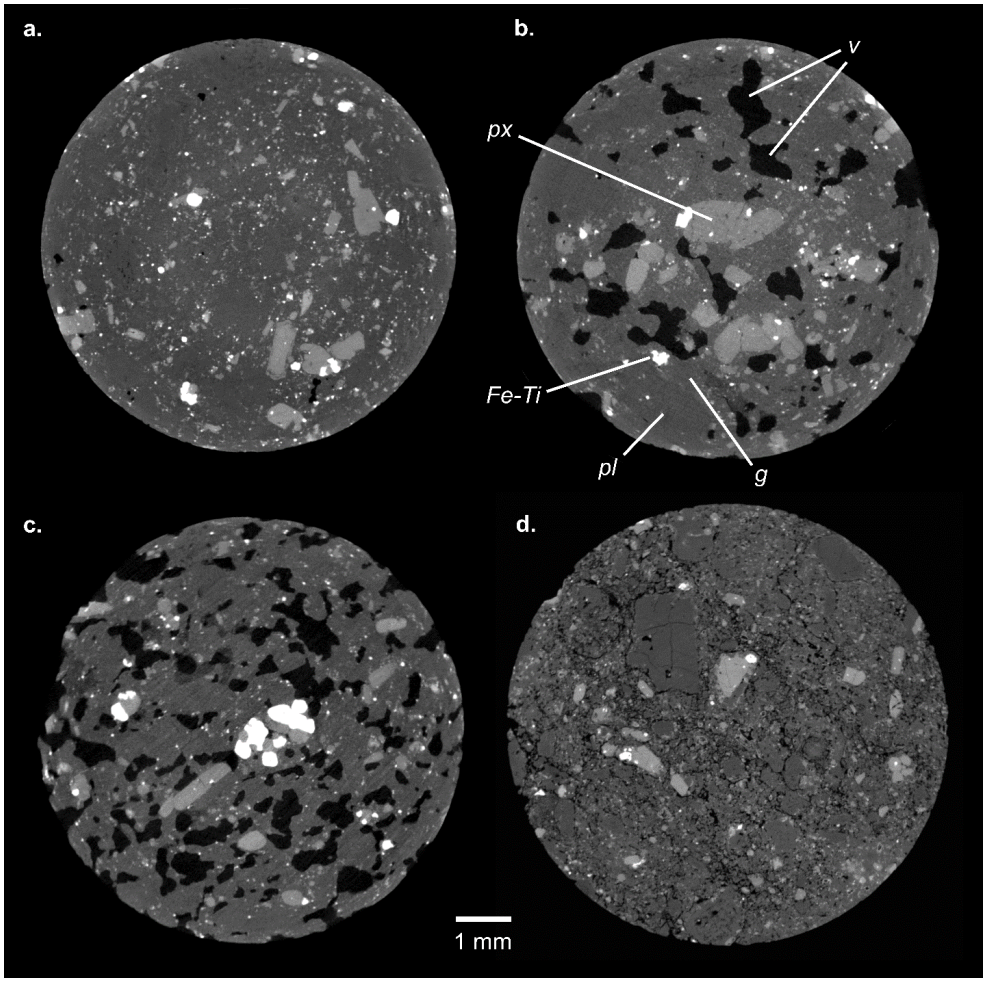

Fig. 5: Examples of reconstructed micro-tomographic slices of different types of samples, which constitute the X-ray micro-tomography data used to measure the properties of the porous network (numerical porosity, pore volumes, throat areas, number densities, tortuosity). Void space (*v*) appears black, plagioclase crystals (*pl*) and glassy groundmass (*g*) appear dark grey, pyroxene crystals (*px*) appear light grey and Fe-Ti oxide crystals (*Fe-Ti*) appear white. **a.** Dense host andesite featuring very few, small void spaces **b.** More porous host andesite showing large polylobate/branching pores **c.** Porous rind of the breadcrust bomb, also showing polylobate/branching pores **d.** Tuffisite sample showing a distinct pore structure characterised by curvilinear voids surrounding a granular solid fraction made up of rounded fragments of the host andesite phases.

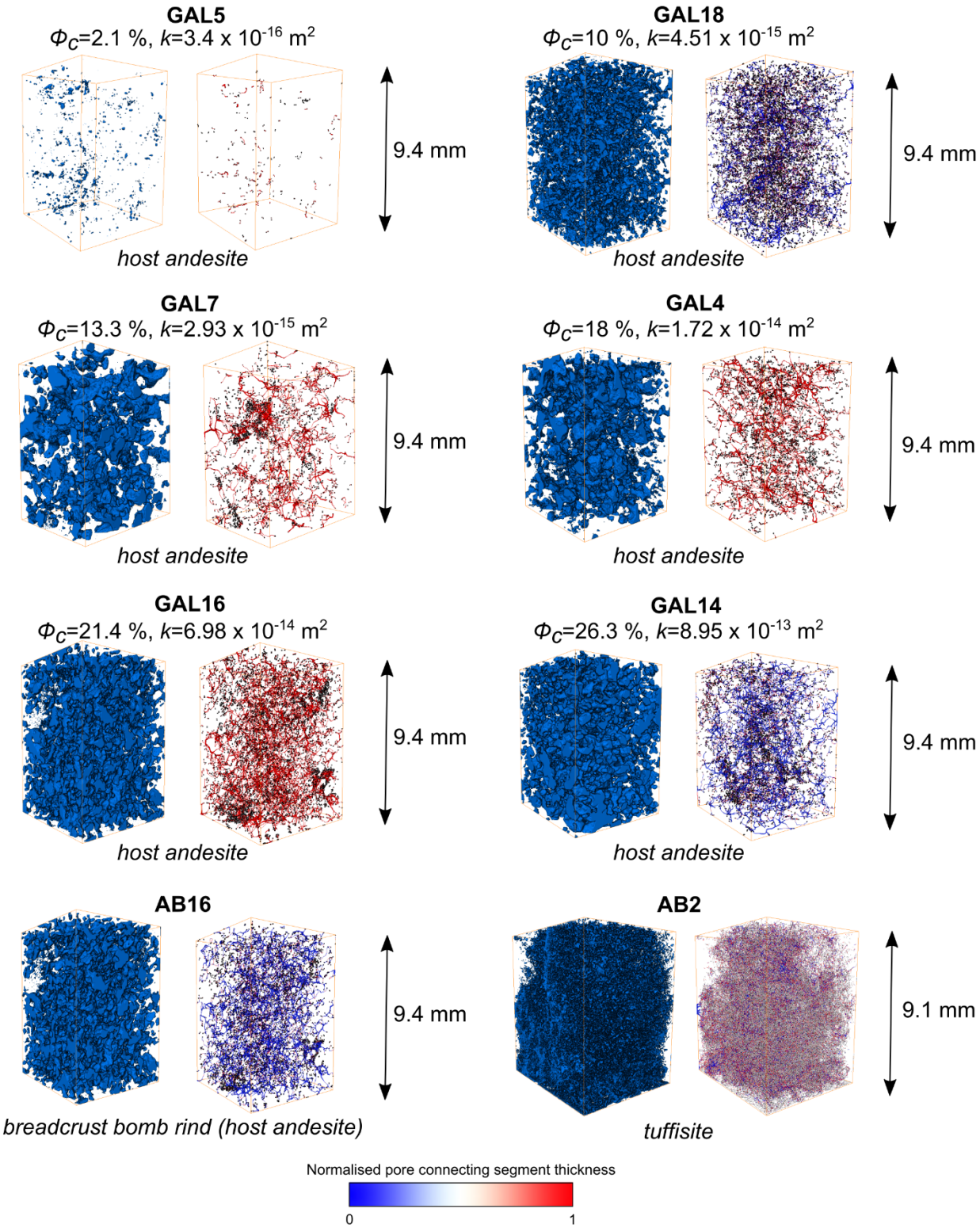

Fig. 6: Rendering of the segmented pore space (left) and pore network model (right) for selected samples covering a range of connected porosities. Segmentation and skeletonisation for the renderings shown here were performed using Avizo software v9, for illustration

purposes only. All quantification of the pore space was performed using 3DMA-Rock (Lindquist & Venkatarangan 1999). The height (measured in the z direction) of each data volume is indicated by the black arrows. In the pore network models shown here, nodal pores are illustrated by black spheres and segments joining nodal pores are shown with thicknesses and colours normalised by the maximum distance from the skeleton to the exterior edge of the pore space object (see colour bar). The connected porosity, ϕ_c, and the permeability, k, (measured at a confining pressure of 0.7 MPa) are given for samples for which these were measured.

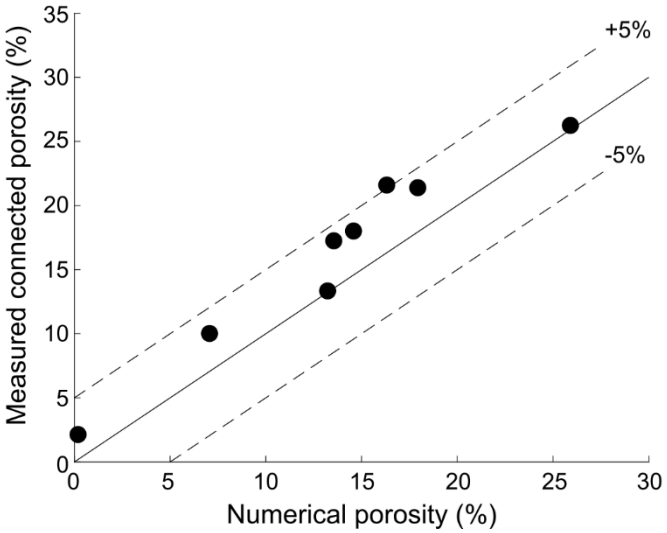

Fig. 7: Comparison of connected porosity measured by pycnometry and total numerical porosity calculated from micro-tomography data. The solid line represents the one-to-one line, with +5 % and -5 % difference indicated by the dashed lines.

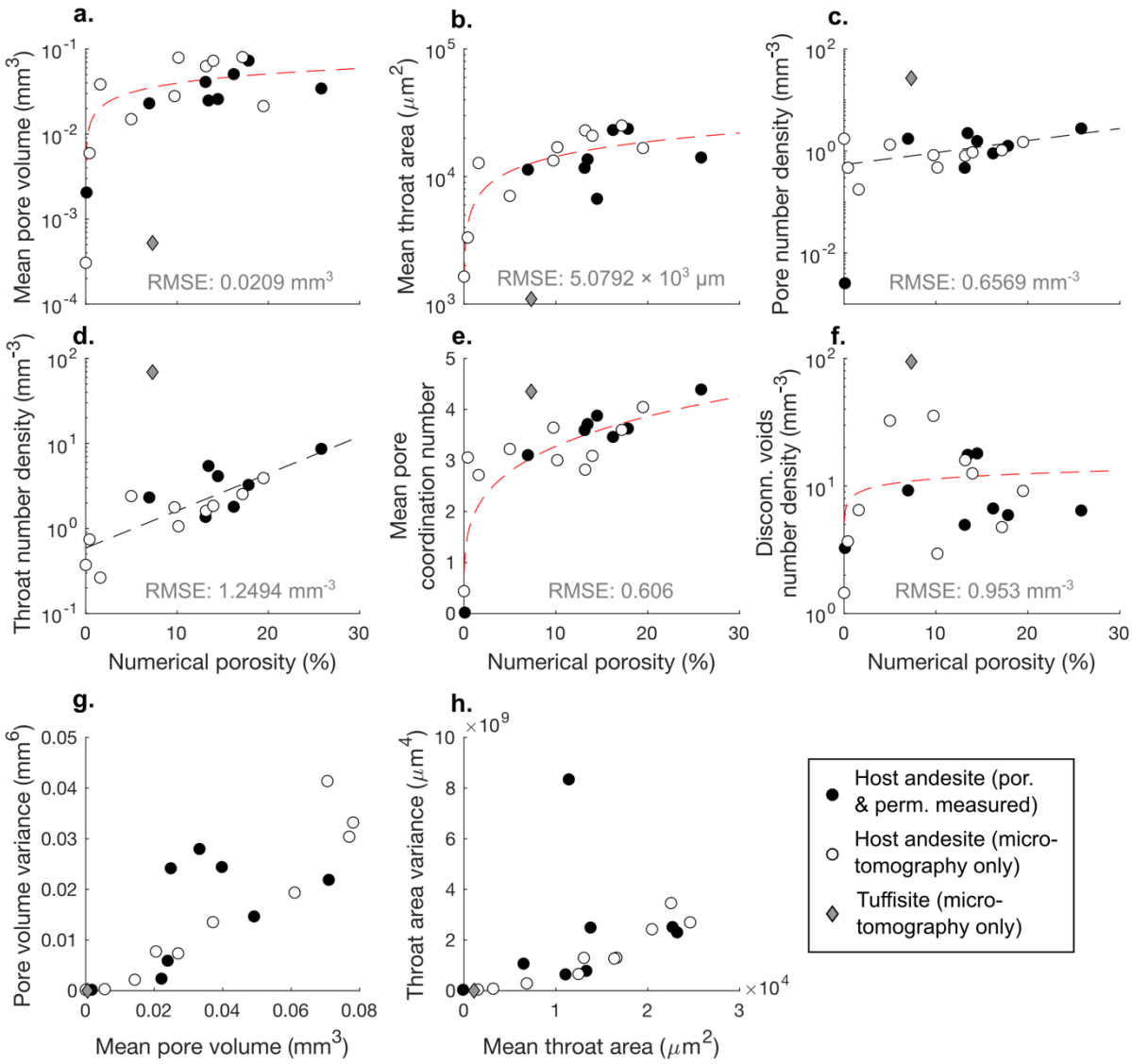

Fig. 8: a–f Micro-tomography results compared with the total numerical porosity calculated for each sample. Dashed lines correspond to the least-squares best-fit power law (red) and exponential (black) functions to highlight overall relationships for the host andesite (RMSE indicated in each panel). Other attempted fits are given in Supplementary File A. Samples of host andesite with lower numerical porosity have smaller mean pore volumes and mean throat areas, lower volumetric number densities of connected pores, throats and disconnected voids, and smaller mean pore coordination numbers. **g–h** Samples with lower mean pore volumes and mean throat areas also have lower pore volume and throat area variances.

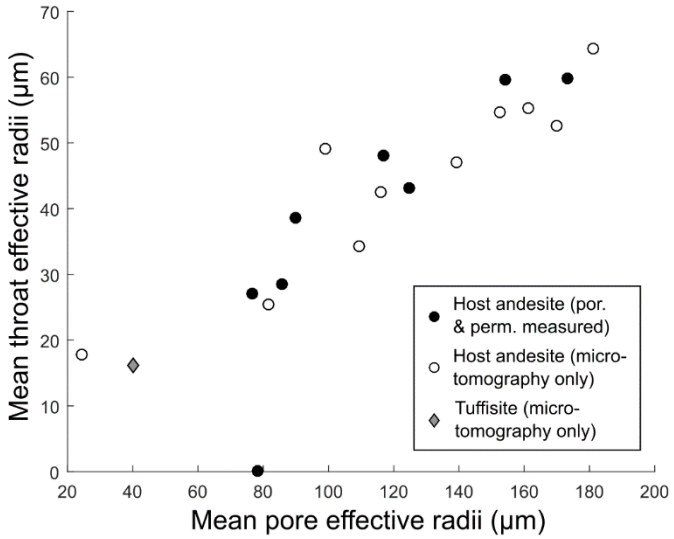

Fig. 9: The mean pore and mean throat effective radii in each sample are positively correlated, showing that samples with small pores have small pore throats and vice-versa. One clear outlier corresponds to dense sample GAL5, where only one pore and zero throats were identified by micro-tomography in the analysed volume after the data cleaning procedure.

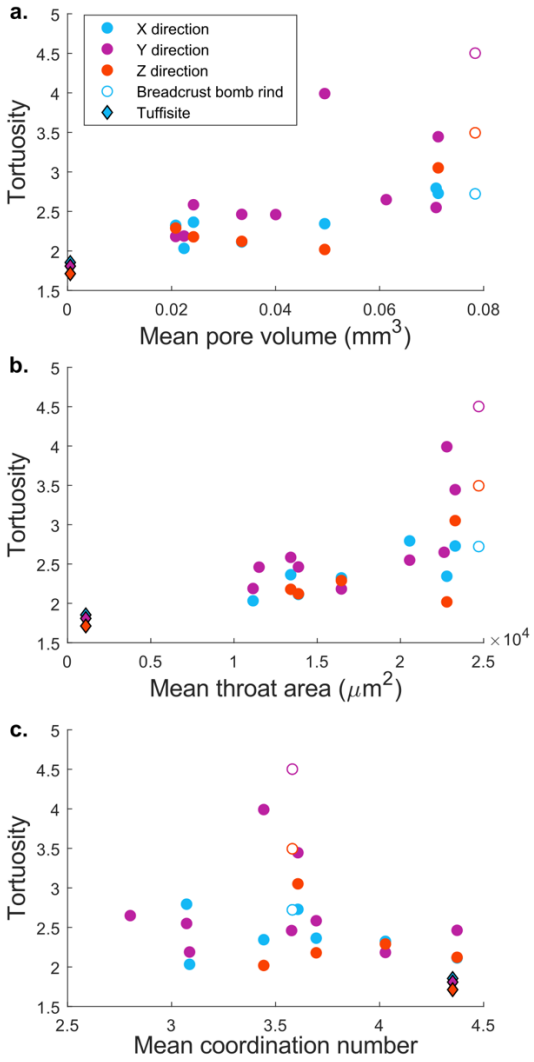

Fig. 10: Median geometric tortuosity measured where possible along connected paths in each direction (x, y and z) of the prismatic volume analysed by micro-tomography. Diamonds correspond to the tuffisite sample and open symbols correspond to the breadcrust bomb rind. Tortuosity is typically lower and more isotropic in samples with lower mean pore volumes and lower mean throat areas. Tortuosity shows no clear relationship with mean pore coordination number. The tuffisite sample shows the lowest tortuosity in the dataset and the breadcrust bomb rind shows the highest anisotropy with respect to tortuosity.

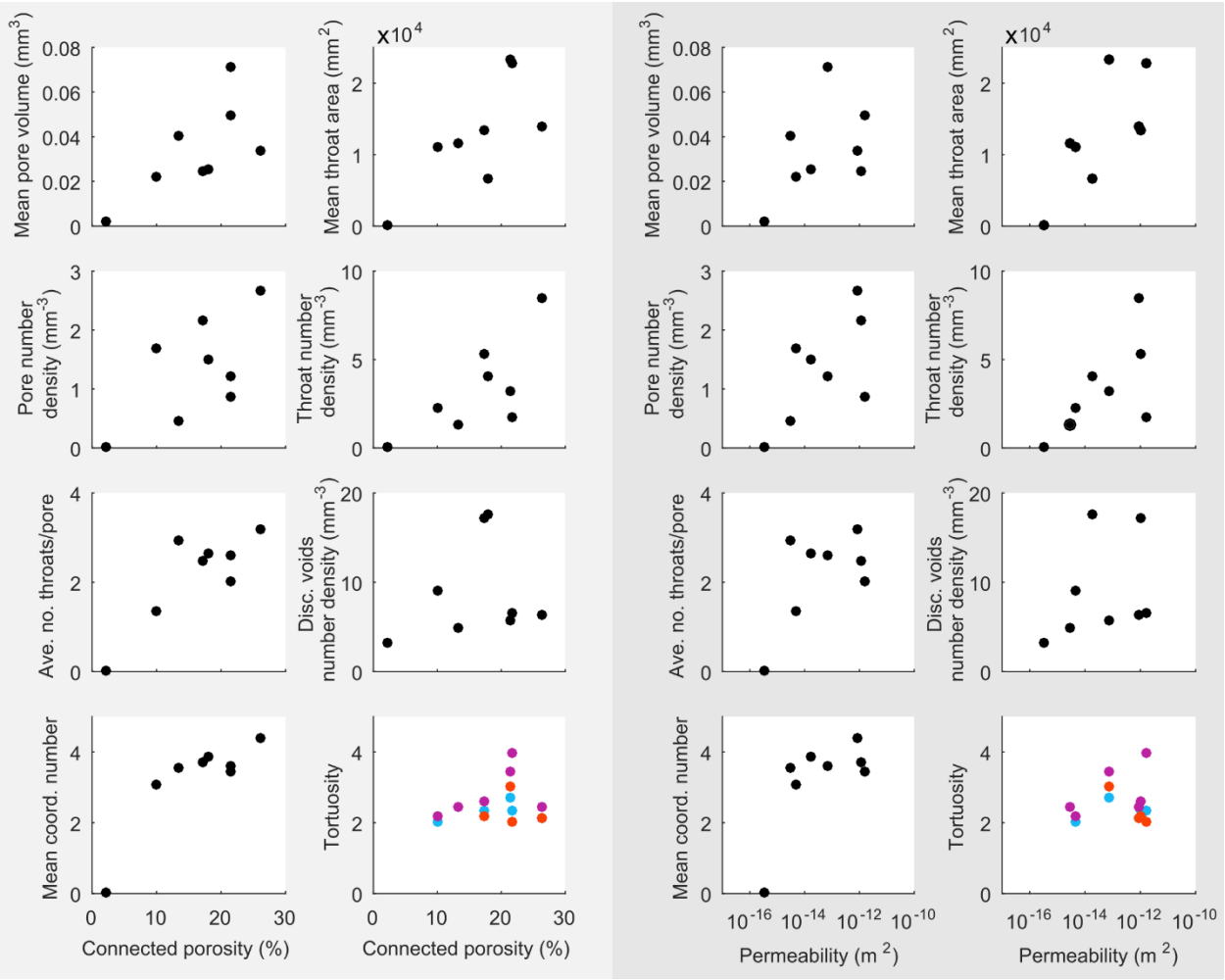

Fig. 11: Micro-tomography results compared with connected porosity, ϕ_c, and permeability, k (measured at a confining pressure of 0.7 MPa). Samples with higher ϕ_c and k typically have higher mean pore volumes and mean throat areas, higher number densities of pores, throats and disconnected voids, a higher ratio of throats to pores per unit volume of analysed material (shown as ave. no. throats/pore), and a higher mean coordination number. Tortuosity decreases slightly with ϕ_c but shows no consistent relationship with k in this sample set (blue indicates tortuosity in the x direction, purple in the y direction and red in the z direction).

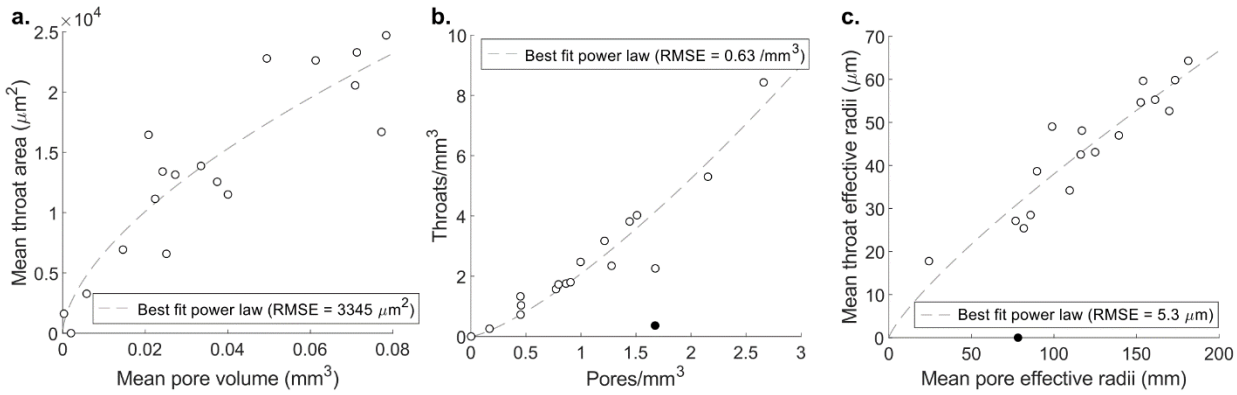

Fig. 12: Fitted curves (grey dashed lines) showing the relationships between key topological parameters **(a–c)** measured by micro-tomography. These relationships reflect the densification process in the high-crystallinity andesites of Galeras volcano. Black filled symbols in panels **b** and **c** denote outliers that were excluded from the fitting procedure (see text).

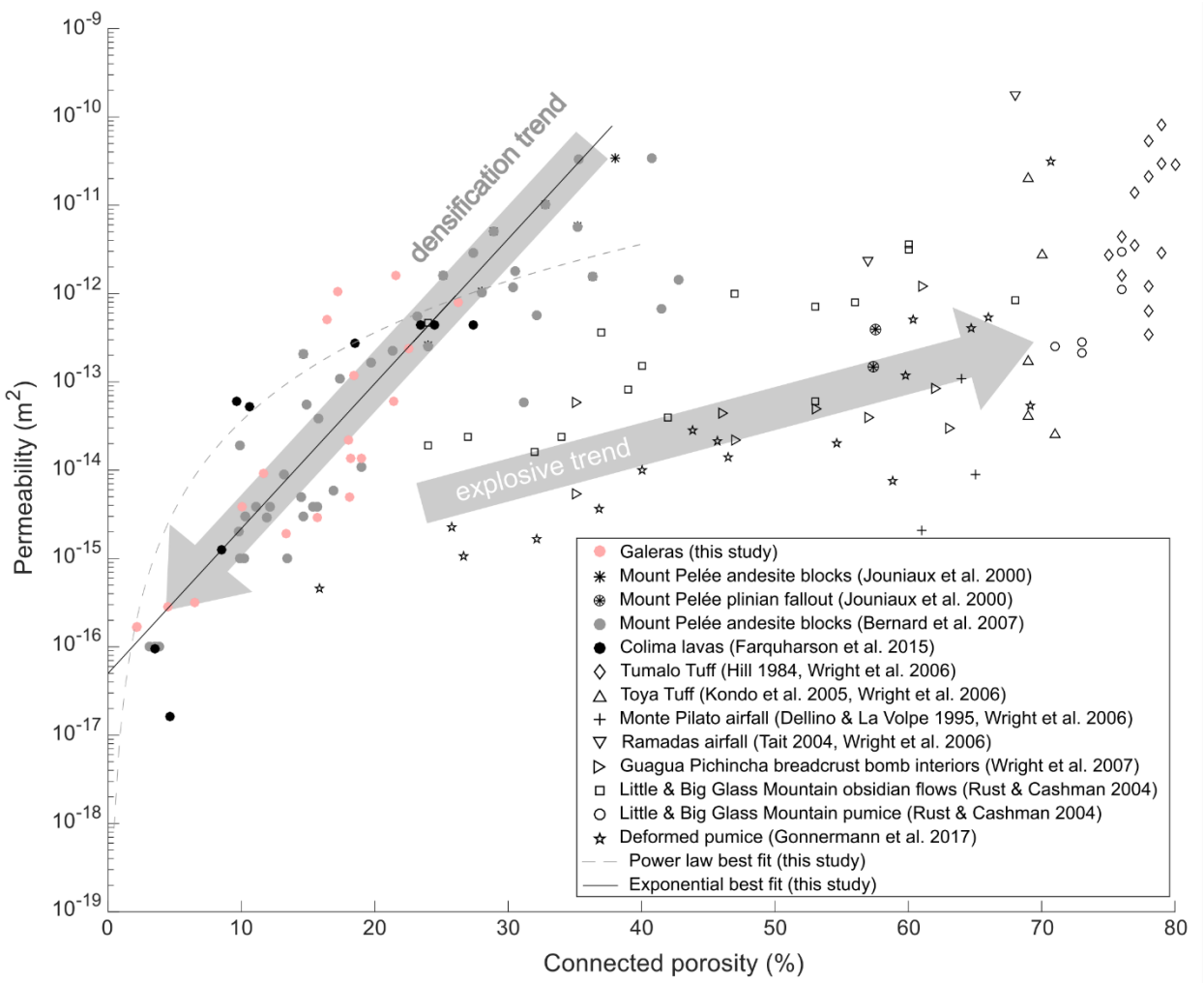

Fig . 13: Porosity and permeability (measured at a confining pressure of 1.4 MPa) data from this study plotted with data from selected effusive (filled symbols) and explosive (open symbols) volcanic products from published studies (see legend). The effusive samples shown here consist of lavas and blocks from block-and-ash flows from andesitic strato-volcanoes. Data from Galeras fit with the overall trend for these types of effusive products and show a higher permeability at lower connected porosities than explosive volcanic products, which follow a distinct trend. Also shown are the best-fit power law and exponential relationships for the Galeras data from this study (see section 4.2).

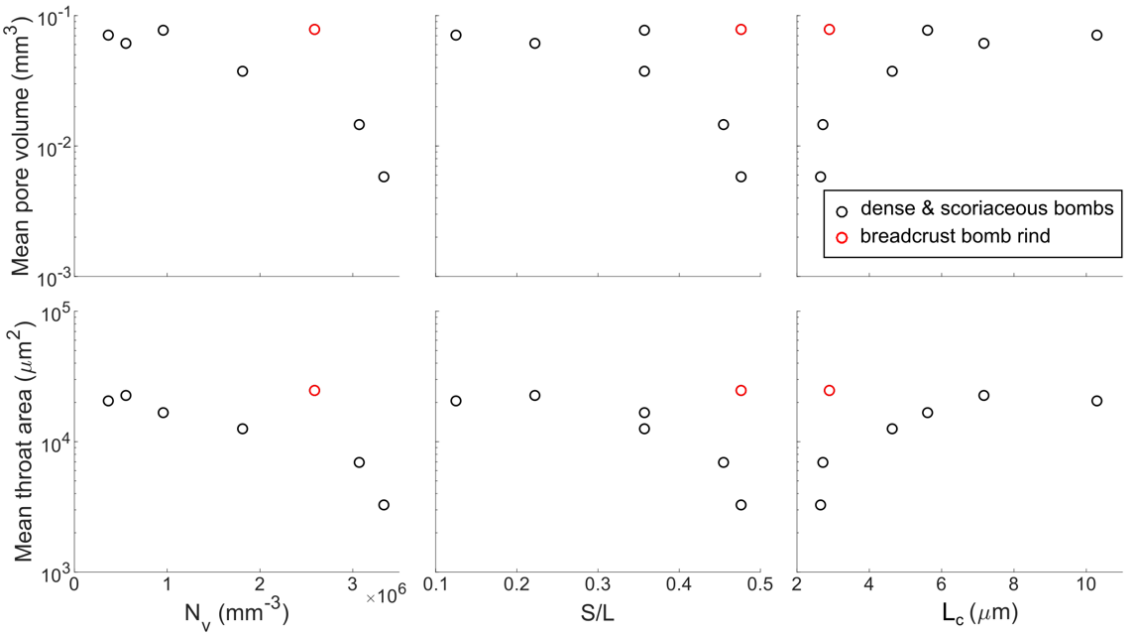

1248

1249 **Fig. 14:** Comparison of micro-tomography results with previously-published crystal micro-
1250 texture results for the same samples from the study of Bain et al. (2019). N_v is the plagioclase
1251 microlite volumetric number density calculated from crystal size distributions, S/L is the best
1252 fit plagioclase microlite aspect ratio (short axis / long axis) and the characteristic microlite
1253 size was calculated from the smallest size bins of the crystal size distributions. Samples with
1254 high N_v, high S/L and small characteristic microlite sizes have micro-textures characterised
1255 by high numbers of small, tabular microlites and show small mean pore volumes and mean
1256 throat areas. Samples with low N_v, low S/L and higher characteristic microlite sizes have
1257 micro-textures characterised by lower numbers of large prismatic microlites and show larger
1258 mean pore volumes and mean throat areas. The breadcrust bomb rind has the largest mean
1259 pore volume and mean throat area, and plots separately from the trend of the dense and
1260 scoriaceous bombs.

1261

1262

1263

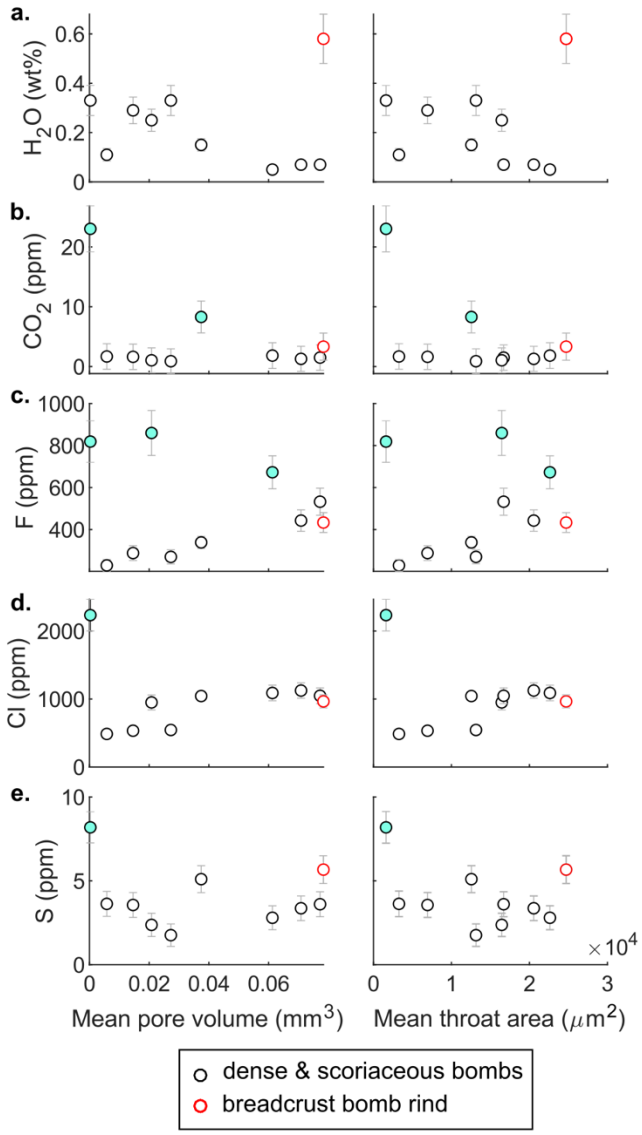

Fig. 15: Comparison of micro-tomography results with previously published groundmass glass volatiles data for the same samples from the study of Bain et al. (2019), where vertical error bars correspond to two sigma. Horizontal error bars for the mean pore volume and mean throat areas are smaller than the symbol size. Outliers interpreted to result from the effects of vapour fluxing are coloured in blue (see section 5.4). Samples with the highest mean pore volumes and mean throat areas tend to have the lowest groundmass glass water content (H_2O) but the highest Fluorine (F) and Chlorine (Cl) content, and vice versa. Carbon dioxide (CO_2) and Sulphur (S) show no relationship with mean pore volume and mean throat area.

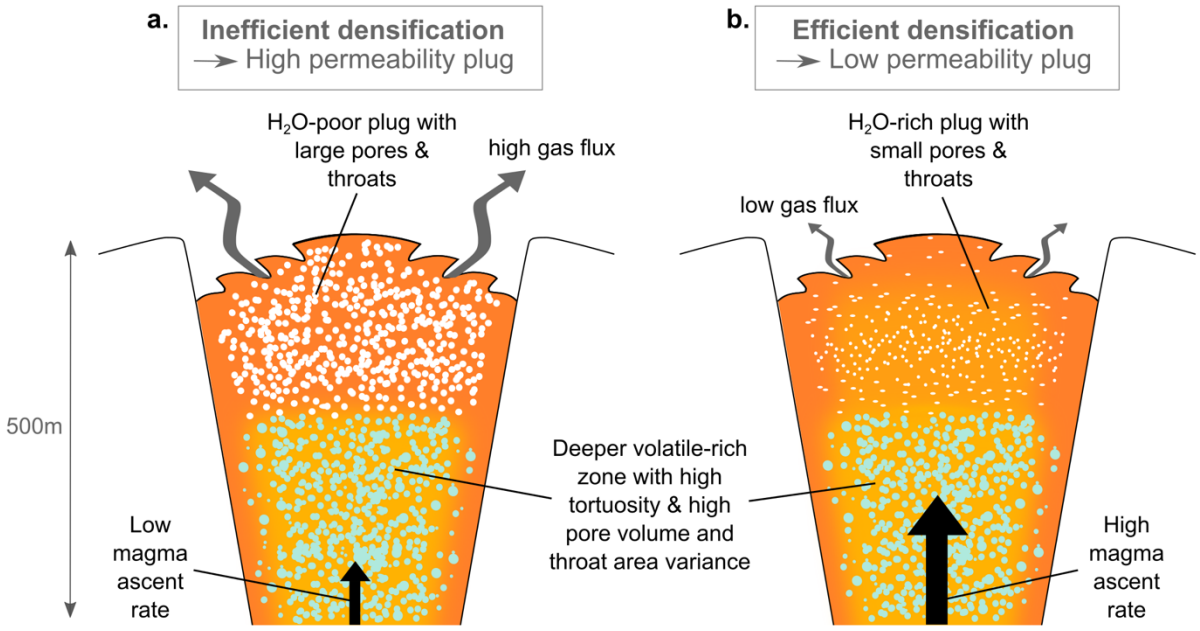

Fig. 16: Conceptual model showing contrasting magma plug structures resulting from different densification efficiencies. **a.** Inefficient densification results from low average ascent and decompression rates, forming relatively high-permeability plugs with an H_2O-poor residual melt phase. **b.** Efficient densification results from high average ascent and decompression rates, forming comparatively low-permeability plugs with a more H_2O-rich residual melt phase.

Tables:

Sample name	Explosion date	Connected porosity ϕ_c (%)	Permeability k (m^2)	Micro-tomography	Crystal micro-textures[1]	Groundmass glass volatiles[1]
GAL1	2004-2010	4.5	3.79×10^{-16}	-	-	-
GAL2	2004-2010	18.1	6.48×10^{-15}	-	-	-
GAL3	2004-2010	22.5	2.83×10^{-13}	-	-	-
GAL4	2004-2010	18	1.72×10^{-14}	y	-	-
GAL5	2004-2010	2.1	3.4×10^{-16}	y	-	-
GAL6	2004-2010	17.3	1.08×10^{-12}	y	-	-
GAL7	2004-2010	13.3	2.93×10^{-15}	y	-	-
GAL8	2004-2010	21.6	1.63×10^{-12}	y	-	-
GAL9	2004-2010	18.2	1.39×10^{-14}	-	-	-
GAL10	2004-2010	1.9	1.13×10^{-16}	-	-	-
GAL11	2004-2010	15.7	3.74×10^{-15}	-	-	-
GAL12	2004-2010	19	1.25×10^{-14}	-	-	-
GAL13	2004-2010	18.4	1.24×10^{-13}	-	-	-
GAL14	2004-2010	26.3	8.95×10^{-13}	y	-	-
GAL15	2004-2010	6.5	4.85×10^{-16}	-	-	-
GAL16	2004-2010	21.4	6.98×10^{-14}	y	-	-
GAL17	2004-2010	11.6	8.50×10^{-15}	-	-	-
GAL18	2004-2010	10	4.51×10^{-15}	y	-	-
GAL19	2004-2010	16.4	5.06×10^{-13}	-	-	-
$AB2_T$	11/12 Aug. 2004	-	-	y	-	-
AB8	12 July 2006	-	-	y	y	y
AB9	12 July 2006	-	-	y	y	y
AB14	17 Jan. 2008	-	-	y	y	y
AB15	17 Jan. 2008	-	-	y	y	y
$AB16_{bb}$	20 Feb. 2009	-	-	y	y	y
AB18	2 Jan. 2010	-	-	y	y	y
AB21	2 Jan. 2010	-	-	y	y	y
AB23	2004-2010	-	-	y	-	y
AB26	2004-2010	-	-	y	-	y
AB37	2004-2010	-	-	y	-	y

[1] Data from Bain et al. (2019). All other data from this study.
$_T$ indicates the tuffisite sample.
$_{bb}$ indicates the breadcrust bomb rind sample.

Table 1: List of samples, connected porosity and permeability (measured at 0.7 MPa confining pressure) measurements and analyses performed. The complete permeability results are provided in Supplementary File B.

Property	**GAL4**	**GAL6**	**GAL16**	**GAL8**
Connected porosity (%)	18	17.3	21.4	21.6
Permeability* (m^2)	1.3-2.22 × 10^{-14}	1.03-1.08 × 10^{-12}	5.58-6.98 × 10^{-14}	1.55-1.63 × 10^{-12}
Mean coordination number	3.86	3.70	3.61	3.44
Number density of disconnected voids (mm^{-3})	17.7	17.2	5.8	6.6
Number density of pores (mm^{-3})	1.5	2.2	1.2	0.9
Number density of throats (mm^{-3})	4	5.3	3.2	1.8
Mean effective pore radius (µm)	77	117	173	154
Mean effective throat radius (µm)	27	48	60	60
Pore volume variance (mm^6)	2.40 × 10^{-2}	5.73 × 10^{-3}	2.17 × 10^{-2}	1.45 × 10^{-2}
Throat area variance ($µm^4$)	1.03 × 10^9	7.47 × 10^8	2.27 × 10^9	2.48 × 10^9
Tortuosity in x/y/z directions	n/a - n/a - n/a	2.36 - 2.58 - 2.18	2.73 - 3.45 - 3.05	2.34 - 3.99 - 2.02

*Permeability measured over the range of confining pressures 0.7-2.1 MPa.

Table 2: Properties of the porous network in two low/high permeability sample pairs with similar connected porosity (GAL4/GAL6 & GAL16/GAL8), calculated from micro-tomography data.